
Implicit Neural Representations with Periodic Activation Functions

Vincent Sitzmann*
sitzmann@cs.stanford.edu

Julien N. P. Martel*
jnmartel@stanford.edu

Alexander W. Bergman
awb@stanford.edu

David B. Lindell
lindell@stanford.edu

Gordon Wetzstein
gordon.wetzstein@stanford.edu

Stanford University
vsitzmann.github.io/siren/

Abstract

Implicitly defined, continuous, differentiable signal representations parameterized by neural networks have emerged as a powerful paradigm, offering many possible benefits over conventional representations. However, current network architectures for such implicit neural representations are incapable of modeling signals with fine detail, and fail to represent a signal’s spatial and temporal derivatives, despite the fact that these are essential to many physical signals defined implicitly as the solution to partial differential equations. We propose to leverage periodic activation functions for implicit neural representations and demonstrate that these networks, dubbed sinusoidal representation networks or SIRENs, are ideally suited for representing complex natural signals and their derivatives. We analyze SIREN activation statistics to propose a principled initialization scheme and demonstrate the representation of images, wavefields, video, sound, and their derivatives. Further, we show how SIRENs can be leveraged to solve challenging boundary value problems, such as particular Eikonal equations (yielding signed distance functions), the Poisson equation, and the Helmholtz and wave equations. Lastly, we combine SIRENs with hypernetworks to learn priors over the space of SIREN functions. Please see the project website for a video overview of the proposed method and all applications.

1 Introduction

We are interested in a class of functions Φ that satisfy equations of the form

$$F(\mathbf{x}, \Phi, \nabla_{\mathbf{x}}\Phi, \nabla_{\mathbf{x}}^2\Phi, \dots) = 0, \quad \Phi : \mathbf{x} \mapsto \Phi(\mathbf{x}). \quad (1)$$

This implicit problem formulation takes as input the spatial or spatio-temporal coordinates $\mathbf{x} \in \mathbb{R}^m$ and, optionally, derivatives of Φ with respect to these coordinates. Our goal is then to learn a neural network that parameterizes Φ to map \mathbf{x} to some quantity of interest while satisfying the constraint presented in Equation (1). Thus, Φ is implicitly defined by the relation defined by F and we refer to neural networks that parameterize such implicitly defined functions as *implicit neural representations*. As we show in this paper, a surprisingly wide variety of problems across scientific fields fall into this form, such as modeling many different types of discrete signals in image, video, and audio processing using a continuous and differentiable representation, learning 3D shape representations via signed distance functions [1–4], and, more generally, solving boundary value problems, such as the Poisson, Helmholtz, or wave equations.

*These authors contributed equally to this work.

A continuous parameterization offers several benefits over alternatives, such as discrete grid-based representations. For example, due to the fact that Φ is defined on the continuous domain of \mathbf{x} , it can be significantly more memory efficient than a discrete representation, allowing it to model fine detail that is not limited by the grid resolution but by the capacity of the underlying network architecture. Being differentiable implies that gradients and higher-order derivatives can be computed analytically, for example using automatic differentiation, which again makes these models independent of conventional grid resolutions. Finally, with well-behaved derivatives, implicit neural representations may offer a new toolbox for solving inverse problems, such as differential equations.

For these reasons, implicit neural representations have seen significant research interest over the last year (Sec. 2). Most of these recent representations build on ReLU-based multilayer perceptrons (MLPs). While promising, these architectures lack the capacity to represent fine details in the underlying signals, and they typically do not represent the derivatives of a target signal well. This is partly due to the fact that ReLU networks are piecewise linear, their second derivative is zero everywhere, and they are thus incapable of modeling information contained in higher-order derivatives of natural signals. While alternative activations, such as tanh or softplus, are capable of representing higher-order derivatives, we demonstrate that their derivatives are often not well behaved and also fail to represent fine details.

To address these limitations, we leverage MLPs with periodic activation functions for implicit neural representations. We demonstrate that this approach is not only capable of representing details in the signals better than ReLU-MLPs, or positional encoding strategies proposed in concurrent work [5], but that these properties also uniquely apply to the derivatives, which is critical for many applications we explore in this paper.

To summarize, the contributions of our work include:

- A continuous implicit neural representation using periodic activation functions that fits complicated signals, such as natural images and 3D shapes, and their derivatives robustly.
- An initialization scheme for training these representations and validation that distributions of these representations can be learned using hypernetworks.
- Demonstration of applications in: image, video, and audio representation; 3D shape reconstruction; solving first-order differential equations that aim at estimating a signal by supervising only with its gradients; and solving second-order differential equations.

2 Related Work

Implicit neural representations. Recent work has demonstrated the potential of fully connected networks as continuous, memory-efficient implicit representations for shape parts [6, 7], objects [1, 4, 8, 9], or scenes [10–13]. These representations are typically trained from some form of 3D data as either signed distance functions [1, 4, 8–12] or occupancy networks [2, 14]. In addition to representing shape, some of these models have been extended to also encode object appearance [3, 5, 10, 15, 16], which can be trained using (multiview) 2D image data using neural rendering [17]. Temporally aware extensions [18] and variants that add part-level semantic segmentation [19] have also been proposed.

Periodic nonlinearities. Periodic nonlinearities have been investigated repeatedly over the past decades, but have so far failed to robustly outperform alternative activation functions. Early work includes Fourier neural networks, engineered to mimic the Fourier transform via single-hidden-layer networks [20, 21]. Other work explores neural networks with periodic activations for simple classification tasks [22–24] and recurrent neural networks [25–29]. It has been shown that such models have universal function approximation properties [30–32]. Compositional pattern producing networks [33, 34] also leverage periodic nonlinearities, but rely on a combination of different nonlinearities via evolution in a genetic algorithm framework. Motivated by the discrete cosine transform, Klocek et al. [35] leverage cosine activation functions for image representation but they do not study the derivatives of these representations or other applications explored in our work. Inspired by these and other seminal works, we explore MLPs with periodic activation functions for applications involving implicit neural representations and their derivatives, and we propose principled initialization and generalization schemes.

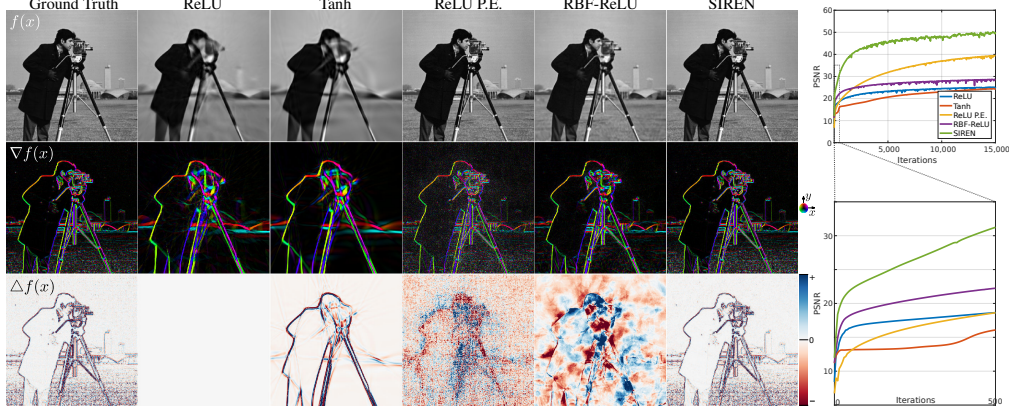


Figure 1: Comparison of different implicit network architectures fitting a ground truth image (top left). The representation is only supervised on the target image but we also show first- and second-order derivatives of the function fit in rows 2 and 3, respectively.

Neural DE Solvers. Neural networks have long been investigated in the context of solving differential equations (DEs) [36], and have previously been introduced as implicit representations for this task [37]. Early work on this topic involved simple neural network models, consisting of MLPs or radial basis function networks with few hidden layers and hyperbolic tangent or sigmoid nonlinearities [37–39]. The limited capacity of these shallow networks typically constrained results to 1D solutions or simple 2D surfaces. Modern approaches to these techniques leverage recent optimization frameworks and auto-differentiation, but use similar architectures based on MLPs. Still, solving more sophisticated equations with higher dimensionality, more constraints, or more complex geometries is feasible [40–42]. However, we show that the commonly used MLPs with smooth, non-periodic activation functions fail to accurately model high-frequency information and higher-order derivatives even with dense supervision.

Neural ODEs [43] are related to this topic, but are very different in nature. Whereas implicit neural representations can be used to directly solve ODEs or PDEs from supervision on the system dynamics, neural ODEs allow for continuous function modeling by pairing a conventional ODE solver (e.g., implicit Adams or Runge-Kutta) with a network that parameterizes the dynamics of a function. The proposed architecture may be complementary to this line of work.

3 Formulation

Our goal is to solve problems of the form presented in Equation (1). We cast this as a feasibility problem, where a function Φ is sought that satisfies a set of M constraints $\{\mathcal{C}_m(\mathbf{a}(\mathbf{x}), \Phi(\mathbf{x}), \nabla\Phi(\mathbf{x}), \dots)\}_{m=1}^M$, each of which relate the function Φ and/or its derivatives to quantities $\mathbf{a}(\mathbf{x})$:

$$\text{find } \Phi(\mathbf{x}) \quad \text{subject to } \mathcal{C}_m(\mathbf{a}(\mathbf{x}), \Phi(\mathbf{x}), \nabla\Phi(\mathbf{x}), \dots) = 0, \forall \mathbf{x} \in \Omega_m, m = 1, \dots, M \quad (2)$$

This problem can be cast in a loss function that penalizes deviations from each of the constraints on their domain Ω_m :

$$\mathcal{L} = \int_{\Omega} \sum_{m=1}^M \mathbf{1}_{\Omega_m}(\mathbf{x}) \|\mathcal{C}_m(\mathbf{a}(\mathbf{x}), \Phi(\mathbf{x}), \nabla\Phi(\mathbf{x}), \dots)\| d\mathbf{x}, \quad (3)$$

with the indicator function $\mathbf{1}_{\Omega_m}(\mathbf{x}) = 1$ when $\mathbf{x} \in \Omega_m$ and 0 when $\mathbf{x} \notin \Omega_m$. In practice, the loss function is enforced by sampling Ω . A dataset $\mathcal{D} = \{(\mathbf{x}_i, \mathbf{a}_i(\mathbf{x}))\}_i$ is a set of tuples of coordinates $\mathbf{x}_i \in \Omega$ along with samples from the quantities $\mathbf{a}(\mathbf{x}_i)$ that appear in the constraints. Thus, the loss in Equation (3) is enforced on coordinates \mathbf{x}_i sampled from the dataset, yielding the loss $\tilde{\mathcal{L}} = \sum_{i \in \mathcal{D}} \sum_{m=1}^M \|\mathcal{C}_m(a(\mathbf{x}_i), \Phi(\mathbf{x}_i), \nabla\Phi(\mathbf{x}_i), \dots)\|$. In practice, the dataset \mathcal{D} is sampled dynamically at training time, approximating \mathcal{L} better as the number of samples grows, as in Monte Carlo integration.

We parameterize functions Φ_θ as fully connected neural networks with parameters θ , and solve the resulting optimization problem using gradient descent.

3.1 Periodic Activations for Implicit Neural Representations

We propose SIREN, a simple neural network architecture for implicit neural representations that uses the sine as a periodic activation function:

$$\Phi(\mathbf{x}) = \mathbf{W}_n (\phi_{n-1} \circ \phi_{n-2} \circ \dots \circ \phi_0)(\mathbf{x}) + \mathbf{b}_n, \quad \mathbf{x}_i \mapsto \phi_i(\mathbf{x}_i) = \sin(\mathbf{W}_i \mathbf{x}_i + \mathbf{b}_i). \quad (4)$$

Here, $\phi_i : \mathbb{R}^{M_i} \mapsto \mathbb{R}^{N_i}$ is the i^{th} layer of the network. It consists of the affine transform defined by the weight matrix $\mathbf{W}_i \in \mathbb{R}^{N_i \times M_i}$ and the biases $\mathbf{b}_i \in \mathbb{R}^{N_i}$ applied on the input $\mathbf{x}_i \in \mathbb{R}^{M_i}$, followed by the sine nonlinearity applied to each component of the resulting vector.

Interestingly, any derivative of a SIREN *is itself a SIREN*, as the derivative of the sine is a cosine, i.e., a phase-shifted sine (see supplemental). Therefore, the derivatives of a SIREN inherit the properties of SIRENs, enabling us to supervise any derivative of SIREN with “complicated” signals. In our experiments, we demonstrate that when a SIREN is supervised using a constraint \mathcal{C}_m involving the derivatives of ϕ , the function ϕ remains well behaved, which is crucial in solving many problems, including boundary value problems (BVPs).

We will show that SIRENs can be initialized with some control over the distribution of activations, allowing us to create deep architectures. Furthermore, SIRENs converge significantly faster than baseline architectures, fitting, for instance, a single image in a few hundred iterations, taking a few seconds on a modern GPU, while featuring higher image fidelity (Fig. 1).

A simple example: fitting an image. Consider the case of finding the function $\Phi : \mathbb{R}^2 \mapsto \mathbb{R}^3, \mathbf{x} \rightarrow \Phi(\mathbf{x})$ that parameterizes a given discrete image f in a continuous fashion. The image defines a dataset $\mathcal{D} = \{(\mathbf{x}_i, f(\mathbf{x}_i))\}_i$ of pixel coordinates $\mathbf{x}_i = (x_i, y_i)$ associated with their RGB colors $f(\mathbf{x}_i)$. The only constraint \mathcal{C} enforces is that Φ shall output image colors at pixel coordinates, solely depending on Φ (none of its derivatives) and $f(\mathbf{x}_i)$, with the form $\mathcal{C}(f(\mathbf{x}_i), \Phi(\mathbf{x})) = \Phi(\mathbf{x}_i) - f(\mathbf{x}_i)$ which can be translated into the loss $\hat{\mathcal{L}} = \sum_i \|\Phi(\mathbf{x}_i) - f(\mathbf{x}_i)\|^2$. In Fig. 1,

we fit Φ_θ using comparable network architectures with different activation functions to a natural image. We supervise this experiment only on the image values, but also visualize the gradients ∇f and Laplacians Δf . While only two approaches, a ReLU network with positional encoding (P.E.) [5] and our SIREN, accurately represent the ground truth image $f(\mathbf{x})$, SIREN is the only network capable of also representing the derivatives of the signal. Additionally, we run a simple experiment where we fit a short video with 300 frames and with a resolution of 512×512 pixels using both ReLU and SIREN MLPs. As seen in Figure 2, our approach is successful in representing this video with an average peak signal-to-noise ratio close to 30 dB, outperforming the ReLU baseline by about 5 dB. We also show the flexibility of SIRENs by representing audio signals in the supplement.

3.2 Distribution of activations, frequencies, and a principled initialization scheme

We present a principled initialization scheme necessary for the effective training of SIRENs. While presented informally here, we discuss further details, proofs and empirical validation in the supplemental material. The key idea in our initialization scheme is to preserve the distribution of activations through the network so that the final output at initialization does not depend on the number of layers. Note that building SIRENs with not carefully chosen uniformly distributed weights yielded poor performance both in accuracy and in convergence speed.

To this end, let us first consider the output distribution of a single sine neuron with the uniformly distributed input $x \sim \mathcal{U}(-1, 1)$. The neuron’s output is $y = \sin(ax + b)$ with $a, b \in \mathbb{R}$. It can be shown that for any $a > \frac{\pi}{2}$, i.e. spanning at least half a period, the output of the sine is $y \sim \text{arcsine}(-1, 1)$, a special case of a U-shaped Beta distribution and independent of the choice of



Figure 2: Example frames from fitting a video with SIREN and ReLU-MLPs. Our approach faithfully reconstructs fine details like the whiskers. Mean (and standard deviation) of the PSNR over all frames is reported.

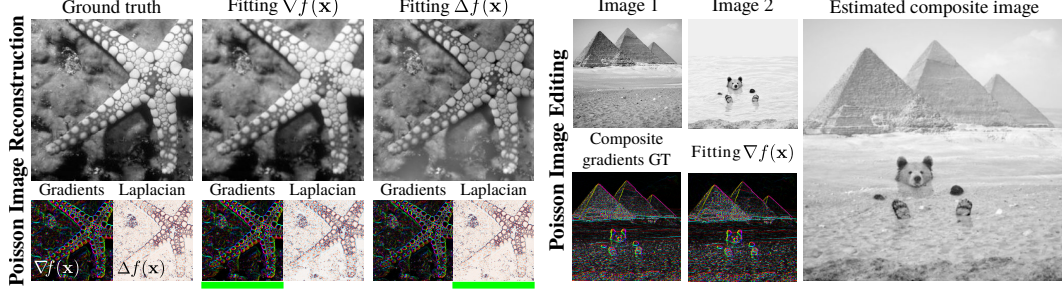


Figure 3: **Poisson image reconstruction:** An image (left) is reconstructed by fitting a SIREN, supervised either by its gradients or Laplacians (underlined in green). The results, shown in the center and right, respectively, match both the image and its derivatives well. **Poisson image editing:** The gradients of two images (top) are fused (bottom left). SIREN allows for the composite (right) to be reconstructed using supervision on the gradients (bottom right).

b. We can now reason about the output distribution of a neuron. Taking the linear combination of n inputs $\mathbf{x} \in \mathbb{R}^n$ weighted by $\mathbf{w} \in \mathbb{R}^n$, its output is $y = \sin(\mathbf{w}^T \mathbf{x} + b)$. Assuming this neuron is in the second layer, each of its inputs is arcsine distributed. When each component of \mathbf{w} is uniformly distributed such as $w_i \sim \mathcal{U}(-c/\sqrt{n}, c/\sqrt{n})$, $c \in \mathbb{R}$, we show (see supplemental) that the dot product converges to the normal distribution $\mathbf{w}^T \mathbf{x} \sim \mathcal{N}(0, c^2/6)$ as n grows. Finally, feeding this normally distributed dot product through another sine is also arcsine distributed for any $c > \sqrt{6}$. Note that the weights of a SIREN can be interpreted as angular frequencies while the biases are phase offsets. Thus, larger frequencies appear in the networks for weights with larger magnitudes. For $|\mathbf{w}^T \mathbf{x}| < \pi/4$, the sine layer will leave the frequencies unchanged, as the sine is approximately linear. In fact, we empirically find that a sine layer keeps spatial frequencies approximately constant for amplitudes such as $|\mathbf{w}^T \mathbf{x}| < \pi$, and increases spatial frequencies for amplitudes above this value².

Hence, we propose to draw weights with $c = 6$ so that $w_i \sim \mathcal{U}(-\sqrt{6/n}, \sqrt{6/n})$. This ensures that the input to each sine activation is normal distributed with a standard deviation of 1. Since only a few weights have a magnitude larger than π , the frequency throughout the sine network grows only slowly. Finally, we propose to initialize the first layer of the sine network with weights so that the sine function $\sin(\omega_0 \cdot \mathbf{W}\mathbf{x} + \mathbf{b})$ spans multiple periods over $[-1, 1]$. We found $\omega_0 = 30$ to work well for all the applications in this work. The proposed initialization scheme yielded fast and robust convergence using the ADAM optimizer for all experiments in this work.

4 Experiments

In this section, we leverage SIRENs to solve challenging boundary value problems using different types of supervision of the derivatives of Φ . We first solve the Poisson equation via direct supervision of its derivatives. We then solve a particular form of the Eikonal equation, placing a unit-norm constraint on gradients, parameterizing the class of signed distance functions (SDFs). SIREN significantly outperforms ReLU-based SDFs, capturing large scenes at a high level of detail. We then solve the second-order Helmholtz partial differential equation, and the challenging inverse problem of full-waveform inversion. Finally, we combine SIRENs with hypernetworks, learning a prior over the space of parameterized functions. All code and data will be made publicly available.

4.1 Solving the Poisson Equation

We demonstrate that the proposed representation is not only able to accurately represent a function and its derivatives, but that it can also be supervised solely by its derivatives, i.e., the model is never presented with the actual function values, but only values of its first or higher-order derivatives.

An intuitive example representing this class of problems is the Poisson equation. The Poisson equation is perhaps the simplest elliptic partial differential equation (PDE) which is crucial in physics

²Formalizing the distribution of output frequencies throughout SIRENs proves to be a hard task and is out of the scope of this work.

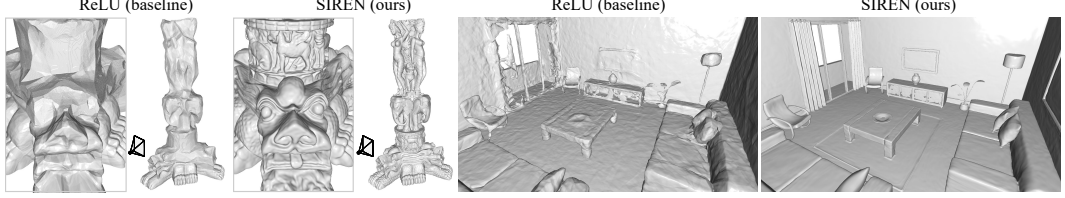


Figure 4: Shape representation. We fit signed distance functions parameterized by implicit neural representations directly on point clouds. Compared to ReLU implicit representations, our periodic activations significantly improve detail of objects (left) and complexity of entire scenes (right).

and engineering, for example to model potentials arising from distributions of charges or masses. In this problem, an unknown ground truth signal f is estimated from discrete samples of either its gradients ∇f or Laplacian $\Delta f = \nabla \cdot \nabla f$ as

$$\mathcal{L}_{\text{grad.}} = \int_{\Omega} \|\nabla_{\mathbf{x}} \Phi(\mathbf{x}) - \nabla_{\mathbf{x}} f(\mathbf{x})\| d\mathbf{x}, \quad \text{or} \quad \mathcal{L}_{\text{lapl.}} = \int_{\Omega} \|\Delta \Phi(\mathbf{x}) - \Delta f(\mathbf{x})\| d\mathbf{x}. \quad (5)$$

Poisson image reconstruction. Solving the Poisson equation enables the reconstruction of images from their derivatives. We show results of this approach using SIREN in Fig. 3. Supervising the implicit representation with either ground truth gradients via $\mathcal{L}_{\text{grad.}}$ or Laplacians via $\mathcal{L}_{\text{lapl.}}$ successfully reconstructs the image. Remaining intensity variations are due to the ill-posedness of the problem.

Poisson image editing. Images can be seamlessly fused in the gradient domain [44]. For this purpose, Φ is supervised using $\mathcal{L}_{\text{grad.}}$ of Eq. (5), where $\nabla_{\mathbf{x}} f(\mathbf{x})$ is a composite function of the gradients of two images $f_{1,2}$: $\nabla_{\mathbf{x}} f(\mathbf{x}) = \alpha \cdot \nabla f_1(x) + (1 - \alpha) \cdot \nabla f_2(x)$, $\alpha \in [0, 1]$. Fig. 3 shows two images seamlessly fused with this approach.

4.2 Representing Shapes with Signed Distance Functions

Inspired by recent work on shape representation with differentiable signed distance functions (SDFs) [1, 4, 9], we fit SDFs directly on oriented point clouds using both ReLU-based implicit neural representations and SIRENs. This amounts to solving a particular Eikonal boundary value problem that constrains the norm of spatial gradients $|\nabla_{\mathbf{x}} \Phi|$ to be 1 almost everywhere. Note that ReLU networks are seemingly ideal for representing SDFs, as their gradients are locally constant and their second derivatives are 0. Adequate training procedures for working directly with point clouds were described in prior work [4, 9]. We fit a SIREN to an oriented point cloud using a loss of the form

$$\mathcal{L}_{\text{sdf}} = \int_{\Omega} \| |\nabla_{\mathbf{x}} \Phi(\mathbf{x})| - 1 \| d\mathbf{x} + \int_{\Omega_0} \|\Phi(\mathbf{x})\| + (1 - \langle \nabla_{\mathbf{x}} \Phi(\mathbf{x}), \mathbf{n}(\mathbf{x}) \rangle) d\mathbf{x} + \int_{\Omega \setminus \Omega_0} \psi(\Phi(\mathbf{x})) d\mathbf{x}, \quad (6)$$

Here, $\psi(\mathbf{x}) = \exp(-\alpha \cdot |\Phi(\mathbf{x})|)$, $\alpha \gg 1$ penalizes off-surface points for creating SDF values close to 0. Ω is the whole domain and we denote the zero-level set of the SDF as Ω_0 . The model $\Phi(\mathbf{x})$ is supervised using oriented points sampled on a mesh, where we require the SIREN to respect $\Phi(\mathbf{x}) = 0$ and its normals $\mathbf{n}(\mathbf{x}) = \nabla f(\mathbf{x})$. During training, each minibatch contains an equal number of points on and off the mesh, each one randomly sampled over Ω . As seen in Fig. 4, the proposed periodic activations significantly increase the details of objects and the complexity of scenes that can be represented by these neural SDFs, parameterizing a full room with only a single five-layer fully connected neural network. This is in contrast to concurrent work that addresses the same failure of conventional MLP architectures to represent complex or large scenes by locally decoding a discrete representation, such as a voxelgrid, into an implicit neural representation of geometry [11–13].

4.3 Solving the Helmholtz and Wave Equations

The Helmholtz and wave equations are second-order partial differential equations related to the physical modeling of diffusion and waves. They are closely related through a Fourier-transform relationship, with the Helmholtz equation given as

$$H(m) \Phi(\mathbf{x}) = -f(\mathbf{x}), \quad \text{with } H(m) = (\Delta + m(\mathbf{x}) w^2). \quad (7)$$

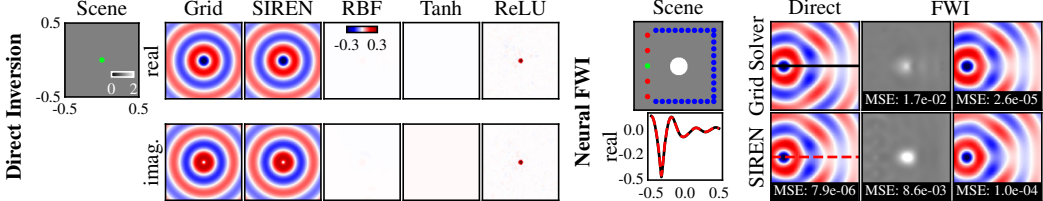


Figure 5: **Direct Inversion:** We solve the Helmholtz equation for a single point source placed at the center of a medium (green dot) with uniform wave propagation velocity (top left). The SIREN solution closely matches a principled grid solver [45] while other network architectures fail to find the correct solution. **Neural Full-Waveform Inversion (FWI):** A scene contains a source (green) and a circular wave velocity perturbation centered at the origin (top left). With the scene velocity known *a priori*, SIREN directly reconstructs a wavefield that closely matches a principled grid solver [45] (bottom left, middle left). For FWI, the velocity and wavefields are reconstructed with receiver measurements (blue dots) from sources triggered in sequence (green, red dots). The SIREN velocity model outperforms a principled FWI solver [46], accurately predicting wavefields. FWI MSE values are calculated across all wavefields and the visualized real wavefield corresponds to the green source.

Here, $f(\mathbf{x})$ represents a known source function, $\Phi(\mathbf{x})$ is the unknown wavefield, and the squared slowness $m(\mathbf{x}) = 1/c(\mathbf{x})^2$ is a function of the wave velocity $c(\mathbf{x})$. In general, the solutions to the Helmholtz equation are complex-valued and require numerical solvers to compute. As the Helmholtz and wave equations follow a similar form, we discuss the Helmholtz equation here, with additional results and discussion for the wave equation in the supplement.

Solving for the wavefield. We solve for the wavefield by parameterizing $\Phi(\mathbf{x})$ with a SIREN. To accommodate a complex-valued solution, we configure the network to output two values, interpreted as the real and imaginary parts. Training is performed on randomly sampled points \mathbf{x} within the domain $\Omega = \{\mathbf{x} \in \mathbb{R}^2 \mid \|\mathbf{x}\|_\infty < 1\}$. The network is supervised using a loss function based on the Helmholtz equation, $\mathcal{L}_{\text{Helmholtz}} = \int_{\Omega} \lambda(\mathbf{x}) \|H(m)\Phi(\mathbf{x}) + f(\mathbf{x})\|_1 d\mathbf{x}$, with $\lambda(\mathbf{x}) = k$, a hyperparameter, when $f(\mathbf{x}) \neq 0$ (corresponding to the inhomogeneous contribution to the Helmholtz equation) and $\lambda(\mathbf{x}) = 1$ otherwise (for the homogenous part). Each minibatch contains samples from both contributions and k is set so the losses are approximately equal at the beginning of training. In practice, we use a slightly modified form of Equation (7) to include the perfectly matched boundary conditions that are necessary to ensure a unique solution [45] (see supplement for details).

Results are shown in Fig. 5 for solving the Helmholtz equation in two dimensions with spatially uniform wave velocity and a single point source (modeled as a Gaussian with $\sigma^2 = 10^{-4}$). The SIREN solution is compared with a principled solver [45] as well as other neural network solvers. All evaluated network architectures use the same number of hidden layers as SIREN but with different activation functions. In the case of the RBF network, we prepend an RBF layer with 1024 hidden units and use a tanh activation. SIREN is the only representation capable of producing a high-fidelity reconstruction of the wavefield. We also note that the tanh network has a similar architecture to recent work on neural PDE solvers [41], except we increase the network size to match SIREN.

Neural full-waveform inversion (FWI). In many wave-based sensing modalities (radar, sonar, seismic imaging, etc.), one attempts to probe and sense across an entire domain using sparsely placed sources (i.e., transmitters) and receivers. FWI uses the known locations of sources and receivers to jointly recover the entire wavefield and other physical properties, such as permittivity, density, or wave velocity. Specifically, the FWI problem can be described as [47]

$$\arg \min_{m, \Phi} \sum_{i=1}^N \int_{\Omega} |\mathcal{H}_r(\Phi_i(\mathbf{x}) - r_i(\mathbf{x}))|^2 d\mathbf{x} \text{ s.t. } H(m) \Phi_i(\mathbf{x}) = -f_i(x), 1 \leq i \leq N, \forall \mathbf{x} \in \Omega, \quad (8)$$

where there are N sources, \mathcal{H}_r samples the wavefield at the receiver locations, and $r_i(x)$ models receiver data for the i th source.

We first use a SIREN to directly solve Eq. 7 for a known wave velocity perturbation, obtaining an accurate wavefield that closely matches that of a principled solver [45] (see Fig. 5, right). Without

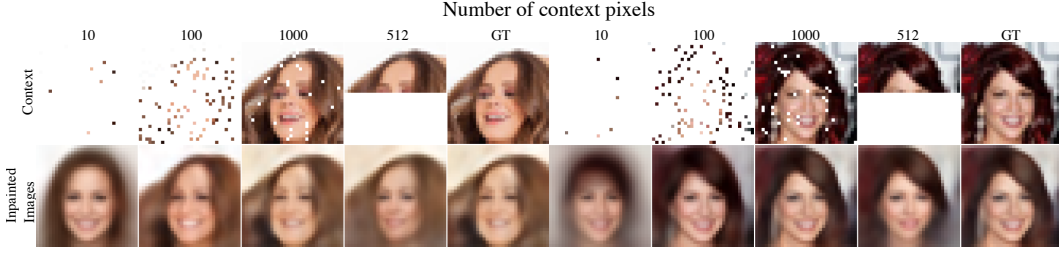


Figure 6: Generalizing across implicit functions parameterized by SIRENs on the CelebA dataset [49]. Image inpainting results are shown for various numbers of context pixels in O_j .

a priori knowledge of the velocity field, FWI is used to jointly recover the wavefields and velocity. Here, we use 5 sources and place 30 receivers around the domain, as shown in Fig. 5. Using the principled solver, we simulate the receiver measurements for the 5 wavefields (one for each source) at a single frequency of 3.2 Hz, which is chosen to be relatively low for improved convergence. We pre-train SIREN to output 5 complex wavefields and a squared slowness value for a uniform velocity. Then, we optimize for the wavefields and squared slowness using a penalty method variation [47] of Eq. 8 (see the supplement for additional details). In Fig. 5, we compare to an FWI solver based on the alternating direction method of multipliers [46, 48]. With only a single frequency for the inversion, the principled solver is prone to converge to a poor solution for the velocity. As shown in Fig. 5, SIREN converges to a better velocity solution and accurate solutions for the wavefields. All reconstructions are performed or shown at 256×256 resolution to avoid noticeable stair-stepping artifacts in the circular velocity perturbation.

4.4 Learning a Space of Implicit Functions

A powerful concept that has emerged for implicit representations is to learn priors over the space of functions that define them [1, 2, 10]. Here we demonstrate that the function space parameterized by SIRENs also admits the learning of powerful priors. Each of these SIRENs Φ_j are fully defined by their parameters $\theta_j \in \mathbb{R}^l$. Assuming that all parameters θ_j of a class exist in a k -dimensional subspace of \mathbb{R}^l , $k < l$, then these parameters can be well modeled by latent code vectors in $\mathbf{z} \in \mathbb{R}^k$. Like in neural processes [50–52], we condition these latent code vectors on partial observations of the signal $O \in \mathbb{R}^m$ through an encoder

$$C : \mathbb{R}^m \rightarrow \mathbb{R}^k, \quad O_j \mapsto C(O_j) = \mathbf{z}_j, \quad (9)$$

and use a ReLU hypernetwork [53], to map the latent code to the weights of a SIREN, as in [10]:

$$\Psi : \mathbb{R}^k \rightarrow \mathbb{R}^l, \quad \mathbf{z}_j \mapsto \Psi(\mathbf{z}_j) = \theta_j. \quad (10)$$

We replicated the experiment from [50] on the CelebA dataset [49] using a set encoder. Additionally, we show results using a convolutional neural network encoder which operates on sparse images. Interestingly, this improves the quantitative and qualitative performance on the inpainting task.

At test time, this enables reconstruction from sparse pixel observations, and, thereby, inpainting. Fig. 6 shows test-time reconstructions from a varying number of pixel observations. Note that these inpainting results were all generated using the same model, with the same parameter values. Tab. 1 reports a quantitative comparison to [50], demonstrating that generalization over SIREN representations is at least equally as powerful as generalization over images.

Table 1: Quantitative comparison to Conditional Neural Processes [50] (CNPs) on the 32×32 CelebA test set. Metrics are reported in pixel-wise mean squared error.

Number of Context Pixels	10	100	1000
CNP [50]	0.039	0.016	0.009
Set Encoder + Hypernet.	0.035	0.013	0.009
CNN Encoder + Hypernet.	0.033	0.009	0.008

5 Discussion and Conclusion

The question of how to represent a signal is at the core of many problems across science and engineering. Implicit neural representations may provide a new tool for many of these by offering a number of potential benefits over conventional continuous and discrete representations. We demonstrate that periodic activation functions are ideally suited for representing complex natural signals and their derivatives using implicit neural representations. We also prototype several boundary value problems that our framework is capable of solving robustly. There are several exciting avenues for future work, including the exploration of other types of inverse problems and applications in areas beyond implicit neural representations, for example neural ODEs [43].

With this work, we make important contributions to the emerging field of implicit neural representation learning and its applications.

Broader Impact

The proposed SIREN representation enables accurate representations of natural signals, such as images, audio, and video in a deep learning framework. This may be an enabler for downstream tasks involving such signals, such as classification for images or speech-to-text systems for audio. Such applications may be leveraged for both positive and negative ends. SIREN may in the future further enable novel approaches to the generation of such signals. This has potential for misuse in impersonating actors without their consent. For an in-depth discussion of such so-called DeepFakes, we refer the reader to a recent review article on neural rendering [17].

Acknowledgments and Disclosure of Funding

Vincent Sitzmann, Alexander W. Bergman, and David B. Lindell were supported by a Stanford Graduate Fellowship. Julien N. P. Martel was supported by a Swiss National Foundation (SNF) Fellowship (P2EZP2 181817). Gordon Wetzstein was supported by an NSF CAREER Award (IIS 1553333), a Sloan Fellowship, and a PECASE from the ARO.

References

- [1] Jeong Joon Park, Peter Florence, Julian Straub, Richard Newcombe, and Steven Lovegrove. Deepsdf: Learning continuous signed distance functions for shape representation. In *Proc. CVPR*, 2019.
- [2] Lars Mescheder, Michael Oechsle, Michael Niemeyer, Sebastian Nowozin, and Andreas Geiger. Occupancy networks: Learning 3d reconstruction in function space. In *Proc. CVPR*, 2019.
- [3] Shunsuke Saito, Zeng Huang, Ryota Natsume, Shigeo Morishima, Angjoo Kanazawa, and Hao Li. Pifu: Pixel-aligned implicit function for high-resolution clothed human digitization. In *Proc. ICCV*, pages 2304–2314, 2019.
- [4] Matan Atzmon and Yaron Lipman. Sal: Sign agnostic learning of shapes from raw data. In *Proc. CVPR*, 2020.
- [5] Ben Mildenhall, Pratul P Srinivasan, Matthew Tancik, Jonathan T Barron, Ravi Ramamoorthi, and Ren Ng. Nerf: Representing scenes as neural radiance fields for view synthesis. *arXiv preprint arXiv:2003.08934*, 2020.
- [6] Kyle Genova, Forrester Cole, Daniel Vlasic, Aaron Sarna, William T Freeman, and Thomas Funkhouser. Learning shape templates with structured implicit functions. In *Proc. ICCV*, pages 7154–7164, 2019.
- [7] Kyle Genova, Forrester Cole, Avneesh Sud, Aaron Sarna, and Thomas Funkhouser. Deep structured implicit functions. *arXiv preprint arXiv:1912.06126*, 2019.
- [8] Mateusz Michalkiewicz, Jhony K Pontes, Dominic Jack, Mahsa Baktashmotagh, and Anders Eriksson. Implicit surface representations as layers in neural networks. In *Proc. ICCV*, pages 4743–4752, 2019.
- [9] Amos Gropp, Lior Yariv, Niv Haim, Matan Atzmon, and Yaron Lipman. Implicit geometric regularization for learning shapes. *arXiv preprint arXiv:2002.10099*, 2020.
- [10] Vincent Sitzmann, Michael Zollhöfer, and Gordon Wetzstein. Scene representation networks: Continuous 3d-structure-aware neural scene representations. In *Proc. NeurIPS*, 2019.
- [11] Chiyu Jiang, Avneesh Sud, Ameesh Makadia, Jingwei Huang, Matthias Nießner, and Thomas Funkhouser. Local implicit grid representations for 3d scenes. In *Proc. CVPR*, pages 6001–6010, 2020.

- [12] Songyou Peng, Michael Niemeyer, Lars Mescheder, Marc Pollefeys, and Andreas Geiger. Convolutional occupancy networks. *arXiv preprint arXiv:2003.04618*, 2020.
- [13] Rohan Chabra, Jan Eric Lenssen, Eddy Ilg, Tanner Schmidt, Julian Straub, Steven Lovegrove, and Richard Newcombe. Deep local shapes: Learning local sdf priors for detailed 3d reconstruction. *arXiv preprint arXiv:2003.10983*, 2020.
- [14] Zhiqin Chen and Hao Zhang. Learning implicit fields for generative shape modeling. In *Proc. CVPR*, pages 5939–5948, 2019.
- [15] Michael Oechsle, Lars Mescheder, Michael Niemeyer, Thilo Strauss, and Andreas Geiger. Texture fields: Learning texture representations in function space. In *Proc. ICCV*, 2019.
- [16] Michael Niemeyer, Lars Mescheder, Michael Oechsle, and Andreas Geiger. Differentiable volumetric rendering: Learning implicit 3d representations without 3d supervision. In *Proc. CVPR*, 2020.
- [17] Ayush Tewari, Ohad Fried, Justus Thies, Vincent Sitzmann, Stephen Lombardi, Kalyan Sunkavalli, Ricardo Martin-Brualla, Tomas Simon, Jason Saragih, Matthias Nießner, et al. State of the art on neural rendering. *Proc. Eurographics*, 2020.
- [18] Michael Niemeyer, Lars Mescheder, Michael Oechsle, and Andreas Geiger. Occupancy flow: 4d reconstruction by learning particle dynamics. In *Proc. ICCV*, 2019.
- [19] Amit Kohli, Vincent Sitzmann, and Gordon Wetzstein. Inferring semantic information with 3d neural scene representations. *arXiv preprint arXiv:2003.12673*, 2020.
- [20] R. Gallant and H. White. There exists a neural network that does not make avoidable mistakes. In *IEEE Int. Conference on Neural Networks*, pages 657–664, 1988.
- [21] Abaylay Zhumeenov, Malika Uteuliyeva, Olzhas Kabdolov, Rustem Takhanov, Zhenisbek Assylbekov, and Alejandro J Castro. Fourier neural networks: A comparative study. *arXiv preprint arXiv:1902.03011*, 2019.
- [22] Josep M Sopena, Enrique Romero, and Rene Alquezar. Neural networks with periodic and monotonic activation functions: a comparative study in classification problems. In *Proc. ICANN*, 1999.
- [23] Kwok-wo Wong, Chi-sing Leung, and Sheng-jiang Chang. Handwritten digit recognition using multilayer feedforward neural networks with periodic and monotonic activation functions. In *Object recognition supported by user interaction for service robots*, volume 3, pages 106–109. IEEE, 2002.
- [24] Giambattista Parascandolo, Heikki Huttunen, and Tuomas Virtanen. Taming the waves: sine as activation function in deep neural networks. 2016.
- [25] Peng Liu, Zhigang Zeng, and Jun Wang. Multistability of recurrent neural networks with nonmonotonic activation functions and mixed time delays. *IEEE Trans. on Systems, Man, and Cybernetics: Systems*, 46(4):512–523, 2015.
- [26] Renée Koplon and Eduardo D Sontag. Using fourier-neural recurrent networks to fit sequential input/output data. *Neurocomputing*, 15(3-4):225–248, 1997.
- [27] M Hisham Choueiki, Clark A Mount-Campbell, and Stanley C Ahalt. Implementing a weighted least squares procedure in training a neural network to solve the short-term load forecasting problem. *IEEE Trans. on Power systems*, 12(4):1689–1694, 1997.
- [28] René Alquézar Mancho. *Symbolic and connectionist learning techniques for grammatical inference*. Universitat Politècnica de Catalunya, 1997.
- [29] JM Sopena and R Alquezar. Improvement of learning in recurrent networks by substituting the sigmoid activation function. In *Proc. ICANN*, pages 417–420. Springer, 1994.
- [30] Emmanuel J Candès. Harmonic analysis of neural networks. *Applied and Computational Harmonic Analysis*, 6(2):197–218, 1999.
- [31] Shaobo Lin, Xiaofei Guo, Feilong Cao, and Zongben Xu. Approximation by neural networks with scattered data. *Applied Mathematics and Computation*, 224:29–35, 2013.
- [32] Sho Sonoda and Noboru Murata. Neural network with unbounded activation functions is universal approximator. *Applied and Computational Harmonic Analysis*, 43(2):233–268, 2017.
- [33] Kenneth O Stanley. Compositional pattern producing networks: A novel abstraction of development. *Genetic programming and evolvable machines*, 8(2):131–162, 2007.
- [34] Alexander Mordvintsev, Nicola Pezzotti, Ludwig Schubert, and Chris Olah. Differentiable image parameterizations. *Distill*, 3(7):e12, 2018.
- [35] Sylwester Klocek, Łukasz Maziarka, Maciej Wołczyk, Jacek Tabor, Jakub Nowak, and Marek Śmieja. Hypernetwork functional image representation. In *Proc. ICANN*, pages 496–510. Springer, 2019.
- [36] Hyuk Lee and In Seok Kang. Neural algorithm for solving differential equations. *Journal of Computational Physics*, 91(1):110–131, 1990.

- [37] Isaac E Lagaris, Aristidis Likas, and Dimitrios I Fotiadis. Artificial neural networks for solving ordinary and partial differential equations. *IEEE Trans. on neural networks*, 9(5):987–1000, 1998.
- [38] Shouling He, Konrad Reif, and Rolf Unbehauen. Multilayer neural networks for solving a class of partial differential equations. *Neural networks*, 13(3):385–396, 2000.
- [39] Nam Mai-Duy and Thanh Tran-Cong. Approximation of function and its derivatives using radial basis function networks. *Applied Mathematical Modelling*, 27(3):197–220, 2003.
- [40] Justin Sirignano and Konstantinos Spiliopoulos. Dgm: A deep learning algorithm for solving partial differential equations. *Journal of Computational Physics*, 375:1339–1364, 2018.
- [41] Maziar Raissi, Paris Perdikaris, and George E Karniadakis. Physics-informed neural networks: A deep learning framework for solving forward and inverse problems involving nonlinear partial differential equations. *Journal of Computational Physics*, 378:686–707, 2019.
- [42] Jens Berg and Kaj Nyström. A unified deep artificial neural network approach to partial differential equations in complex geometries. *Neurocomputing*, 317:28–41, 2018.
- [43] Tian Qi Chen, Yulia Rubanova, Jesse Bettencourt, and David K Duvenaud. Neural ordinary differential equations. In *Proc. NIPS*, pages 6571–6583, 2018.
- [44] Patrick Pérez, Michel Gangnet, and Andrew Blake. Poisson image editing. *ACM Trans. on Graphics*, 22(3):313–318, 2003.
- [45] Zhongying Chen, Dongsheng Cheng, Wei Feng, and Tingting Wu. An optimal 9-point finite difference scheme for the helmholtz equation with pml. *International Journal of Numerical Analysis & Modeling.*, 10(2), 2013.
- [46] Hossein S Aghamiry, Ali Gholami, and Stéphane Operto. Improving full-waveform inversion by wavefield reconstruction with the alternating direction method of multipliers. *Geophysics*, 84(1):R139–R162, 2019.
- [47] Tristan Van Leeuwen and Felix J Herrmann. Mitigating local minima in full-waveform inversion by expanding the search space. *Geophysical Journal International*, 195(1):661–667, 2013.
- [48] Stephen Boyd, Neal Parikh, Eric Chu, Borja Peleato, Jonathan Eckstein, et al. Distributed optimization and statistical learning via the alternating direction method of multipliers. *Foundations and Trends® in Machine learning*, 3(1):1–122, 2011.
- [49] Ziwei Liu, Ping Luo, Xiaogang Wang, and Xiaoou Tang. Deep learning face attributes in the wild. In *Proc. ICCV*, December 2015.
- [50] Marta Garnelo, Dan Rosenbaum, Chris J Maddison, Tiago Ramalho, David Saxton, Murray Shanahan, Yee Whye Teh, Danilo J Rezende, and SM Eslami. Conditional neural processes. *arXiv preprint arXiv:1807.01613*, 2018.
- [51] SM Ali Eslami, Danilo Jimenez Rezende, Frederic Besse, Fabio Viola, Ari S Morcos, Marta Garnelo, Avraham Ruderman, Andrei A Rusu, Ivo Danihelka, Karol Gregor, et al. Neural scene representation and rendering. *Science*, 360(6394):1204–1210, 2018.
- [52] Hyunjik Kim, Andriy Mnih, Jonathan Schwarz, Marta Garnelo, Ali Eslami, Dan Rosenbaum, Oriol Vinyals, and Yee Whye Teh. Attentive neural processes. *Proc. ICLR*, 2019.
- [53] David Ha, Andrew Dai, and Quoc V Le. Hypernetworks. In *Proc. ICLR*, 2017.

Implicit Neural Representations with Periodic Activation Functions

–Supplementary Material–

Vincent Sitzmann*
sitzmann@cs.stanford.edu **Julien N. P. Martel***
jnmartel@stanford.edu **Alexander W. Bergman**
awb@stanford.edu

David B. Lindell
lindell@stanford.edu **Gordon Wetzstein**
gordon.wetzstein@stanford.edu

Stanford University
vsitzmann.github.io/siren/

Contents

1 Initialization and Distribution of Activations	3
1.1 Informal statement	3
1.2 Preliminary results	3
1.3 Formal statement and proof of the initialization scheme	6
1.4 Empirical evaluation	6
1.5 About ω_0	6
2 Evaluating the Gradient of a SIREN is Evaluating another SIREN	6
3 Solving the Poisson Equation	8
3.1 Architecture Comparisons	8
3.2 Implementation & Reproducibility Details	9
4 Representing Shapes with Signed Distance Functions	9
5 Solving the Helmholtz and Wave Equations	10
5.1 Helmholtz Perfectly Matched Layer Formulation	10
5.2 Full-Waveform Inversion	11
5.3 Helmholtz Implementation & Reproducibility Details	11
5.4 Wave Equation Formulation	12
5.5 Solving the Wave Equation	12
5.6 Wave Equation Implementation & Reproducibility Details	12

*These authors contributed equally to this work.

6 Application to Image Processing	13
6.1 Formulation	13
6.2 Image Fitting.	13
6.3 Image Inpainting	14
6.4 Implementation & Reproducibility Details	14
7 Representing Video	16
7.1 Reproducibility & Implementation Details	16
8 Representing Audio Signals	17
8.1 Reproducibility & Implementation Details	18
9 Learning a Space of Implicit Functions	18
9.1 Reproducibility & Implementation Details	18
9.2 Additional Results	20
10 References	21

1 Initialization and Distribution of Activations

1.1 Informal statement

Initialization schemes have been shown to be crucial in the training procedure of deep neural networks [20, 18]. Here, we propose an initialization scheme for SIREN that preserves the distribution of activations through its layers and thus allows us to build deep architectures.

Statement of the initialization scheme. We propose to draw weights according to a uniform distribution $W \sim \mathcal{U}(-\sqrt{6/\text{fan_in}}, \sqrt{6/\text{fan_in}})$. We claim that this leads to the input of each sine activation being Gauss-Normal distributed, and the output of each sine activation approximately arcsine-distributed with a standard deviation of 0.5. Further, we claim that the form as well as the moments of these distributions do not change as the depth of the network grows.

Overview of the proof. Our initialization scheme relies on the fact that if the input to a neuron in a layer is distributed the same way as its output, then by a simple recursive argument we can see that the distributions will be preserved throughout the network.

Hence, we consider an input in the interval $[-1, 1]$. We assume it is drawn uniformly at random, since we interpret it as a “normalized coordinate” in our applications. We first show in **Lemma 1.1**, that pushing this input through a sine nonlinearity yields an arcsine distribution. The second layer (and, as we will show, all following layers), computes a linear combination of such arcsine distributed outputs (of known variance, **Lemma 1.3**). Following Lindeberg’s condition for the central limit theorem, this linear combination will be normal distributed **Lemma 1.5**, with a variance that can be calculated using the variance of the product of random variables (**Lemma 1.4**). It remains to show that pushing a Gaussian distribution through the sine nonlinearity again yields an arcsine distributed output **Lemma 1.6**, and thereby, we may apply the same argument to the distributions of activations of the following layers.

We formally present the lemmas and their proof in the next section before formally stating the initialization scheme and proving it in Section 1.3. We show empirically that the theory predicts very well the behaviour of the initialization scheme in Section 1.4.

1.2 Preliminary results

First let us note that the sine function is periodic, of period 2π and odd: $\sin(-x) = -\sin(x)$, i.e. it is symmetric with respect to the origin. Since we are interested in mapping “coordinates” through SIREN, we will consider an input as a random variable X uniformly distributed in $[-1, 1]$. We will thus study, without loss of generality, the frequency scaled SIREN that uses the activation $\sin(\frac{\pi}{2}x)$. Which is half a period (note that the distribution does not change on a full period, it is “just” considering twice the half period).

Definition 1.1. *The arcsine distribution is defined for a random variable X by its cumulative distribution function (CDF) F_X such as*

$$X \sim \text{Arcsin}(a, b), \text{ with CDF: } F_X(x) = \frac{2}{\pi} \arcsin\left(\sqrt{\frac{x-a}{b-a}}\right), \text{ with } b > a.$$

Lemma 1.1. *Given $X \sim \mathcal{U}(-1, 1)$, and $Y = \sin(\frac{\pi}{2}X)$ we have $Y \sim \text{Arcsin}(-1, 1)$.*

Proof. The cumulative distribution function (CDF) $F_X(x) = \mathbb{P}(X \leq x)$ is defined, for a random variable that admits a continuous probability density function (PDF), f as the integral $F_X(x) = \int_{-\infty}^x f(t) dt$. Hence, for the uniform distribution $\mathcal{U}(-1, 1)$ which is $f(x) = \frac{1}{2}$ over the interval $[-1, 1]$ and 0 everywhere else, it is easy to show that: $F_X(x) = \frac{1}{2}x + \frac{1}{2}$.

We are interested in the distribution of the output $Y = \sin(\frac{\pi}{2}X)$. Noting that $\sin(\frac{\pi}{2})$ is bijective on $[-1, 1]$, we have

$$F_Y(y) = \mathbb{P}\left(\sin\left(\frac{\pi}{2}X\right) \leq y\right) = \mathbb{P}\left(X \leq \frac{2}{\pi} \arcsin y\right) = F_X\left(\frac{2}{\pi} \arcsin y\right),$$

Substituting the CDF F_X , noting it is the uniform distribution which has a compact support (this is $[-1,1]$), we have

$$F_Y(y) = \frac{1}{\pi} \arcsin y + \frac{1}{2}.$$

Using the identity $\arcsin \sqrt{x} = \frac{1}{2} \arcsin(2x - 1) + \frac{\pi}{4}$, we conclude:

$$F_Y(y) \sim \text{Arcsin}(-1, 1).$$

The PDF can be found, deriving the cdf: $f_Y(y) = \frac{d}{dy} F_Y(y) = \frac{1}{\pi} \frac{1}{\sqrt{1-y^2}}$. \square

Lemma 1.2. *The variance of $mX + n$ with X a random variable and $m \in \mathbb{R}_{>0}$, $n \in \mathbb{R}$ is $\text{Var}[mX + n] = m^2 \text{Var}[X]$.*

Proof. For any random variable with a continuous pdf f_X , its expectation is defined as $E[X] = \int_{-\infty}^{\infty} f_X(x)dx$. The variance is defined as $\text{Var}[X] = E[(X - E[X])^2] = E[X^2] - E[X]^2$. Thus, we have $\text{Var}[mX + n] = E[(mX + n)^2] - E[mX + n]^2 = E[m^2 X^2 + 2mnX + n^2] - (mE[X] + n)^2 = m^2(E[X^2] - E[X]^2) = m^2 \text{Var}[X]$. \square

Lemma 1.3. *The variance of $X \sim \text{Arcsin}(a, b)$ is $\text{Var}[X] = \frac{1}{8}(b - a)^2$.*

Proof. First we prove that if $Z \sim \text{Arcsin}(0, 1)$ then $\text{Var}[Z] = \frac{1}{8}$. We have $E[Z] = \frac{1}{2}$ by symmetry, and $\text{Var}[Z] = E[Z^2] - E[Z]^2 = E[Z^2] - \frac{1}{4}$. Remains to compute:

$$E[Z^2] = \int_0^1 z^2 \cdot \frac{1}{\pi \sqrt{z(1-z)}} dz = \frac{2}{\pi} \int_0^1 \frac{t^4}{\sqrt{1-t^2}} dt = \frac{2}{\pi} \int_0^{\pi/2} \sin^4 u du = \frac{3}{8},$$

using a first change of variable: $z = t^2$, $dz = 2t dt$ and then a second change of variable $t = \sin(u)$, $dt = \cos(u)du$. The integral of $\sin^4(u)$ is calculated remarking it is $(\sin^2(u))^2$, and using the formulas of the double angle: $\cos(2u) = 2\cos^2(u) - 1 = 1 - 2\sin^2(u)$.

Second, we prove that if $X \sim \text{Arcsin}(\alpha, \beta)$ then the linear combination $mX + n \sim \text{Arcsin}(\alpha m + n, \beta m + n)$ with $m \in \mathbb{R}_{>0}$, $n \in \mathbb{R}$, (using the same method as in **Lemma 1.1** with $Y = mX + n$).

Posing $X = mZ + n$ and using $n = a$ and $m = b - a$, we have $X \sim \text{Arcsin}(m \cdot 0 + n, m \cdot 1 + n) = \text{Arcsin}(a, b)$. Finally, $\text{Var}[X] = \text{Var}[m \cdot Z + n] = m^2 \cdot \text{Var}[Z] = (b - a)^2 \cdot \frac{1}{8}$ (**Lemma 1.2**). \square

Lemma 1.4. *For two independent random variables X and Y*

$$\text{Var}[X \cdot Y] = \text{Var}[X] \cdot \text{Var}[Y] + E[Y]^2 \cdot \text{Var}[X] + E[X]^2 \cdot \text{Var}[Y].$$

Proof. See [19]. \square

Theorem 1.5. *Central Limit Theorem with Lindeberg's sufficient condition.* Let X_k , $k \in \mathbb{N}$ be independent random variables with expected values $E[X_k] = \mu_k$ and variances $\text{Var}[X_k] = \sigma_k^2$. Posing $s_n^2 = \sum_{k=1}^n \sigma_k^2$. If the X_k statisfy the Lindenberg condition:

$$\lim_{n \rightarrow \infty} \frac{1}{s_n^2} \sum_{k=1}^n E[(X_k - \mu_k)^2 \cdot \mathbf{1}(|X_k - \mu_k| > \epsilon s_n)] = 0 \quad (1)$$

$\forall \epsilon > 0$, then the Central Limit Theorem (CLT) holds. That is,

$$S_n = \frac{1}{s_n} \sum_{k=1}^n (X_k - \mu_k), \quad (2)$$

converges in distribution to the standard normal distribution as $n \rightarrow \infty$.

Proof. See [26, 2]. \square

Lemma 1.6. *Given a Gaussian distributed random variable $X \sim \mathcal{N}(0, 1)$ and $Y = \sin \frac{\pi}{2} X$ we have $Y \sim \text{Arcsin}(-1, 1)$.*

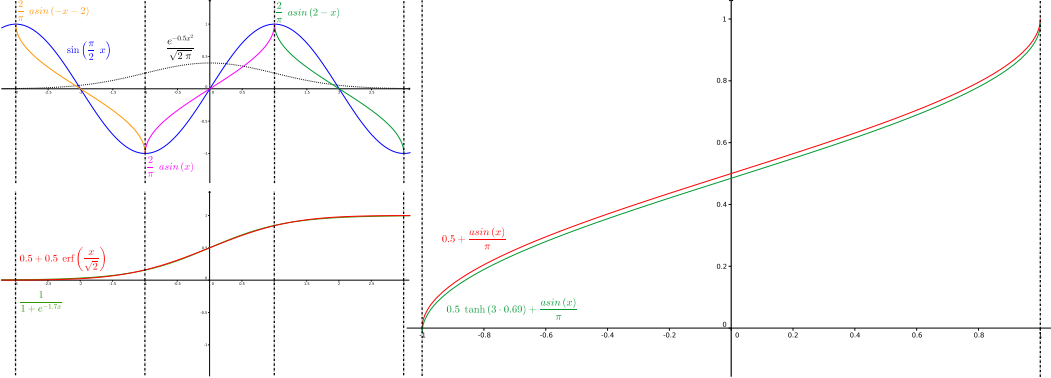


Figure 1: **Top left:** A plot of the standard normal distribution on $[-3, 3]$ as well as the graph of $y = \sin \frac{\pi}{2}x$ and its three reciprocal bijections $y = \frac{2}{\pi} \arcsin(-x - 2)$, $y = \frac{2}{\pi} \arcsin x$ and $y = \frac{2}{\pi} \arcsin(2 - x)$ covering the interval $[-3, 3]$ in which 99.7% of the probability mass of the standard normal distribution lies. **Bottom left:** Plot of the approximation of the CDF of the standard normal with a logistic function. **Right:** Comparison of the theoretically derived CDF of the output of a sine nonlinearity (green) and the ground-truth Arcsine CDF (red), demonstrating that a standard normal distributed input fed to a sine indeed yields an approximately Arcsine distributed output.

Proof. For a random variable X normally distributed we can approximate the CDF of its normal distribution with the logistic function, as in [10]:

$$\begin{aligned} F_X(x) &= \frac{1}{2} + \frac{1}{2} \operatorname{erf}\left(\frac{x}{\sqrt{2}}\right) \\ &\approx (1 + \exp(-\alpha \cdot x))^{-1} \\ &\approx \frac{1}{2} + \frac{1}{2} \tanh(\beta \cdot x), \end{aligned}$$

with $\alpha = 1.702$ and $\beta = 0.690$. Similar to the proof of Lemma (1.1), we are looking for the CDF of the random variable $Y \sim \sin\left(\frac{\pi}{2}X\right)$. However, the normal distribution does not have compact support. This infinite support yields an infinite series describing the CDF of Y .

Hence, we make a second approximation that consists in approximating the CDF of Y on the interval $[-3, 3]$. Because $X \sim \mathcal{N}(0, 1)$, we know that 99.7% of the probability mass of X lies on the compact set $[-3, 3]$. Thus, ignoring the other contributions, we have:

$$\begin{aligned} F_Y(y) &= \mathbb{P}\left(\sin\left(\frac{\pi}{2}X\right) \leq y\right) \\ &= F_X(3) - F_X\left(2 - \frac{2}{\pi} \arcsin x\right) + F_X\left(\frac{2}{\pi} \arcsin x\right) - F_X\left(-\frac{2}{\pi} \arcsin x - 2\right). \end{aligned}$$

Using the logistic approximation of the CDF of X , this is:

$$\begin{aligned} F_X(x) &= \frac{1}{2} \tanh(3\beta) \\ &+ \frac{1}{2} \left(\tanh\left(\frac{2\beta}{\pi}z\right) - \tanh\left(2\beta\left(1 - \frac{1}{\pi}z\right)\right) - \tanh\left(-2\beta\left(1 + \frac{1}{\pi}z\right)\right) \right), \end{aligned}$$

with $z = \arcsin x$. Using a taylor expansion in $z = 0$ (and noting that $\arcsin 0 = 0$) we have:

$$F_X(x) \stackrel{0}{=} \frac{1}{2} \tanh(3\beta) + \frac{1}{\pi} \cdot \arcsin x,$$

which approximates $X \sim \text{Arcsin}(-1, 1)$. Figure 1 illustrates the different steps of the proofs and the approximations we made. \square

Lemma 1.7. *The variance of $X \sim \mathcal{U}(-a, b)$ is $\operatorname{Var}[X] = \frac{1}{12}(b - a)^2$*

Proof. $E[X] = \frac{a+b}{2}$. $\operatorname{Var}[X] = E[X^2] - E[X]^2 = \frac{1}{b-a}[\frac{x^3}{3}]_a^b - (\frac{a+b}{2})^2 = \frac{1}{b-a} \frac{b^3 - a^3}{3} - (\frac{a+b}{2})^2$, developing the cube as $b^3 - a^3 = (b - a)(a^2 + ab + b^2)$ and simplifying yields the result. \square

1.3 Formal statement and proof of the initialization scheme

Theorem 1.8. *For a uniform input in $[-1, 1]$, the activations throughout a SIREN are standard normal distributed before each sine nonlinearity and arcsine-distributed after each sine nonlinearity, irrespective of the depth of the network, if the weights are distributed uniformly in the interval $[-c, c]$ with $c = \sqrt{6/\text{fan_in}}$ in each layer.*

Proof. Assembling all the lemma, a sketch of the proof is:

- Each output X_l for the layer l is $X_l \sim \text{Arcsin}(-1, 1)$ (first layer: from a uniform distribution **Lemma 1.1**, next layers: from a standard-normal **Lemma 1.6** and $\text{Var}[X_l] = \frac{1}{2}$ (**Lemma 1.3**)).
- The input to the layer $l + 1$ is $w_l^T X_l = \sum_i^n w_{i,l} X_{i,l}$ (bias does not change distribution for high enough frequency). Using weights $w_i^l \sim \mathcal{U}(-c, c)$ we have $\text{Var}[w_l^T X_l] = \text{Var}[w_l] \cdot \text{Var}[X_l] = \frac{1}{12}(2c)^2 \cdot \frac{1}{2} = \frac{1}{6}c^2$ (from the variance of a uniform distribution **Lemma 1.7**, and an arcsine distribution **Lemma 1.3**, as well as their product **Lemma 1.4**).
- Choosing $c = \sqrt{\frac{6}{n}}$, with the fan-in n (see dot product above) and using the CLT with weak Lindenberg's condition we have $\text{Var}[w_l^T X_l] = n \cdot \frac{1}{6} \frac{6}{n} = 1$ **Lemma 1.5** and $w_l^T X_l \sim \mathcal{N}(0, 1)$
- This holds true for all layers, since normal distribution through the sine non-linearity yields again the arcsine distribution **Lemma 1.2**, **Lemma 1.6**

□

1.4 Empirical evaluation

We validate our theoretical derivation with an experiment. We assemble a 6-layer, single-input SIREN with 2048 hidden units, and initialize it according to the proposed initialization scheme. We draw 2^8 inputs in a linear range from -1 to 1 and plot the histogram of activations after each linear layer and after each sine activation. We further compute the 1D Fast Fourier Transform of all activations in a layer. Lastly, we compute the sum of activations in the final layer and compute the gradient of this sum w.r.t. each activation. The results can be visualized in Figure 2. The distribution of activations nearly perfectly matches the predicted Gauss-Normal distribution after each linear layer and the arcsine distribution after each sine nonlinearity. As discussed in the main text, frequency components of the spectrum similarly remain comparable, with the maximum frequency growing only slowly. We verified this initialization scheme empirically for a 50-layer SIREN with similar results. Finally, similar to the distribution of activations, we plot the distribution of gradients and empirically demonstrate that it stays almost perfectly constant across layers, demonstrating that SIREN does not suffer from either vanishing or exploding gradients at initialization. We leave a formal investigation of the distribution of gradients to future work.

1.5 About ω_0

As discussed above, we aim to provide each sine nonlinearity with activations that are standard normal distributed, except in the case of the first layer, where we introduced a factor ω_0 that increased the spatial frequency of the first layer to better match the frequency spectrum of the signal. However, we found that the training of SIREN can be accelerated by leveraging a factor ω_0 in *all* layers of the SIREN, by factorizing the weight matrix \mathbf{W} as $\mathbf{W} = \hat{\mathbf{W}} * \omega_0$, choosing $\hat{\mathbf{W}} \sim \mathcal{U}(-\sqrt{\frac{c}{\omega_0^2 n}}, \sqrt{\frac{c}{\omega_0^2 n}})$.

This keeps the distribution of activations constant, but boosts gradients to the weight matrix $\hat{\mathbf{W}}$ by the factor ω_0 while leaving gradients w.r.t. the input of the sine neuron unchanged.

2 Evaluating the Gradient of a SIREN is Evaluating another SIREN

We can write a loss L between a target and a SIREN output as:

$$L(\text{target}, (\mathbf{W}_n \circ \phi_{n-1} \circ \phi_{n-2} \dots \phi_0)(\mathbf{x}) + \mathbf{b}_n). \quad (3)$$

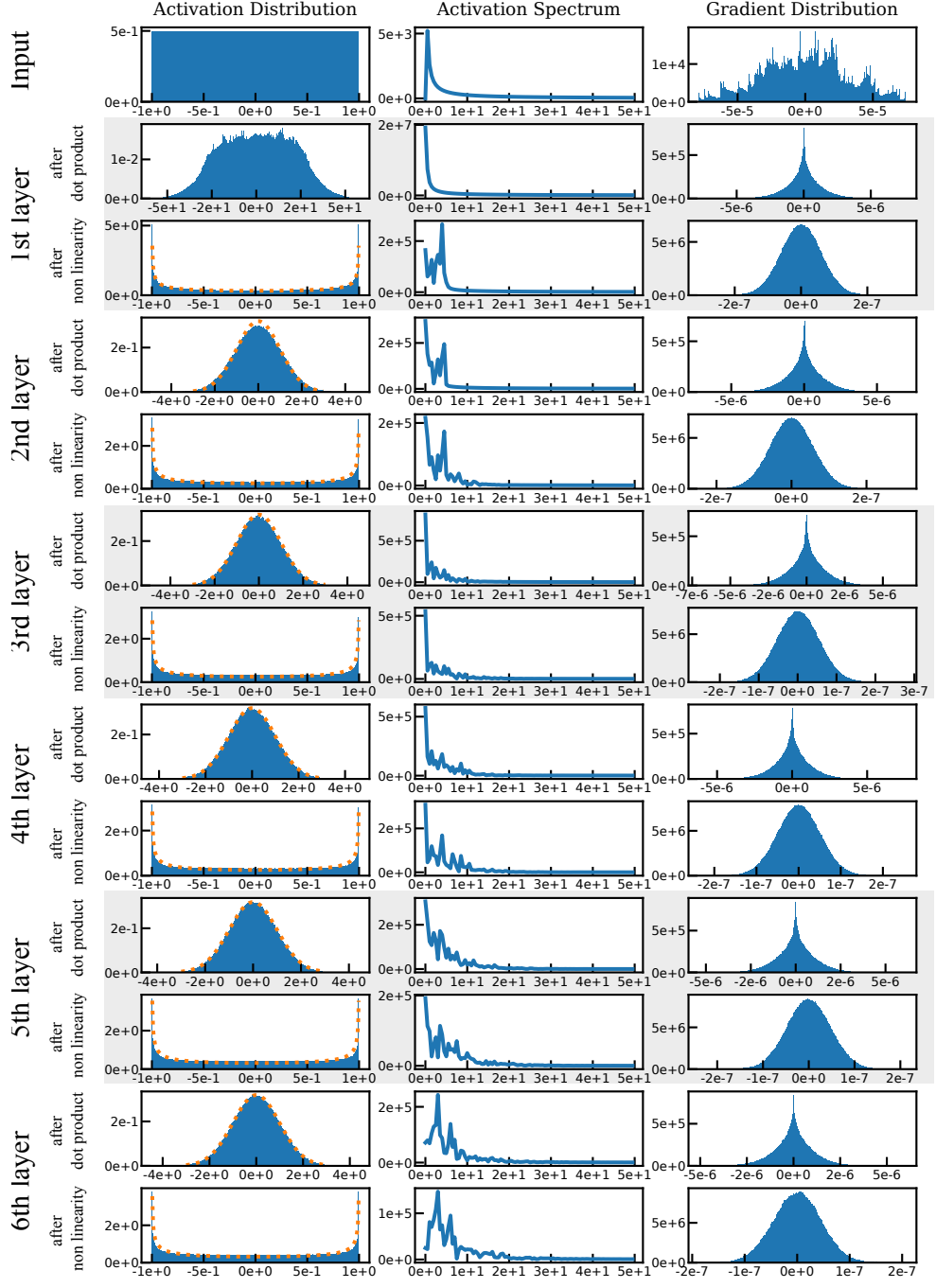


Figure 2: Activation and gradient statistics at initialization for a 6-layer SIREN. Increasing layers from top to bottom. Orange dotted line visualizes analytically predicted distributions. Note how the experiment closely matches theory, activation distributions stay consistent from layer to layer, the maximum frequency throughout layers grows only slowly, and gradient statistics similarly stay consistent from layer to layer.

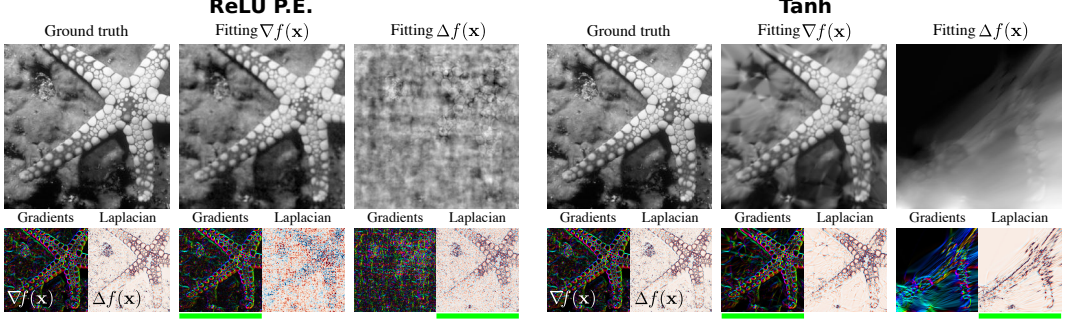


Figure 3: Poisson image reconstruction using the ReLU P.E. (left) and tanh (right) network architectures. For both architectures, image reconstruction from the gradient is of lower quality than SIREN, while reconstruction from the Laplacian is not at all accurate.

A sine layer is defined as:

$$\phi_i(\mathbf{x}) = (\sin \circ \mathbf{T}_i)(\mathbf{x}), \quad \text{with } \mathbf{T}_i : \mathbf{x} \mapsto \mathbf{W}_i \mathbf{x} + \mathbf{b}_i = \hat{\mathbf{W}}_i \hat{\mathbf{x}}, \quad (4)$$

defining $\hat{\mathbf{W}} = [\mathbf{W}, \mathbf{b}]$ and $\hat{\mathbf{x}} = [\mathbf{x}, 1]$ for convenience.

The gradient of the loss with respect to the input can be calculated using the chain rule:

$$\begin{aligned} \nabla_{\mathbf{x}} L &= \left(\frac{\partial L}{\partial \mathbf{y}_n} \cdot \frac{\partial \mathbf{y}_n}{\partial \mathbf{y}_{n-1}} \cdots \frac{\partial \mathbf{y}_1}{\partial \mathbf{y}_0} \cdot \frac{\partial \mathbf{y}_0}{\partial \mathbf{x}} \right)^T \\ &= (\hat{\mathbf{W}}_0^T \cdot \sin'(\mathbf{y}_0)) \cdots (\hat{\mathbf{W}}_{n-1}^T \cdot \sin'(\mathbf{y}_{n-1})) \cdot \hat{\mathbf{W}}_n^T \cdot L'(\mathbf{y}_n) \end{aligned} \quad (5)$$

where $\mathbf{y}_l(\hat{\mathbf{x}})$ is defined as the network evaluated on input $\hat{\mathbf{x}}$ stopping before the non-linearity of layer l , ($\hat{\mathbf{x}}$ is implicit in Equation (5) for the sake of readability):

$$\begin{aligned} \mathbf{y}_0(\hat{\mathbf{x}}) &= \hat{\mathbf{W}}_0 \hat{\mathbf{x}} \\ \mathbf{y}_l(\hat{\mathbf{x}}) &= (\hat{\mathbf{W}}_l \circ \sin)(\mathbf{y}_{l-1}) = (\hat{\mathbf{W}}_l \circ \sin \circ \dots \hat{\mathbf{W}}_0)(\hat{\mathbf{x}}) \end{aligned} \quad (6)$$

Remark that the derivative $\sin'(\mathbf{y}_l) = \cos(\mathbf{y}_l) = \sin(\mathbf{y}_l + \frac{\pi}{2})$, and that we can absorb the $\frac{\pi}{2}$ phase offset in the bias by defining the new weight matrix $\check{\mathbf{W}} = [\mathbf{W}, \mathbf{b} + \frac{\pi}{2}]$. The gradient can be rewritten:

$$\nabla_{\mathbf{x}} L = (\hat{\mathbf{W}}_0^T \cdot \sin(\check{\mathbf{y}}_0)) \cdots (\hat{\mathbf{W}}_{n-1}^T \cdot \sin(\check{\mathbf{y}}_{n-1})) \cdot \hat{\mathbf{W}}_n^T \cdot L'(\mathbf{y}_n) \quad (7)$$

with $\check{\mathbf{y}}_l$ the activations using the weights $\check{\mathbf{W}}_l$

$$\begin{aligned} \check{\mathbf{y}}_0(\hat{\mathbf{x}}) &= \check{\mathbf{W}}_0 \hat{\mathbf{x}} \\ \check{\mathbf{y}}_l(\hat{\mathbf{x}}) &= (\check{\mathbf{W}}_l \circ \sin)(\mathbf{y}_{l-1}) = (\check{\mathbf{W}}_l \circ \sin \circ \dots \check{\mathbf{W}}_0)(\hat{\mathbf{x}}) \end{aligned} \quad (8)$$

which is a forward pass evaluating a slightly different SIREN in which all the biases have been shifted by $\frac{\pi}{2}$.

Furthermore, in Equation (7) since every term of the form $\sin(\mathbf{y}_l)$ is a SIREN, and those terms are multiplied by weight matrices between them, this shows that the gradient of a SIREN can be evaluated by yet another SIREN. It also shows that a SIREN of L layers, requires the evaluation of a SIREN of $\frac{L(L+1)}{2}$ layers.

3 Solving the Poisson Equation

3.1 Architecture Comparisons

To show that our representation is unique in being able to represent signals while being supervised solely by their derivatives, we test other neural network architectures and activation functions on the Poisson image reconstruction task. We show that the performance of the ReLU P.E. network

Table 1: Quantitative comparison of reconstructed image, gradient image, and Laplace image in the Poisson image reconstruction task on the starfish image. Reconstruction accuracy is reported in PSNR after the images have been colorized and normalized.

Model Supervised on	Tanh		ReLU P.E.		SIREN	
	Grad.	Laplacian	Grad.	Laplacian	Grad.	Laplacian
Reconstructed Image	25.79	7.11	26.35	11.14	32.91	14.95
Reconstructed Grad.	19.11	11.14	19.33	11.35	46.85	23.45
Reconstructed Laplacian	18.59	16.35	14.24	18.31	19.88	57.13

architecture, which performed best on the single image fitting task besides SIREN, is not as accurate in supervising on derivatives. This is shown in Fig. 3. Additionally, in Tab. 1, we compare the PSNR of the reconstructed image, gradient image, and Laplace image between various architectures for Poisson image reconstruction.

One interesting observation from Tab. 1 is that other architectures such as ReLU P.E. have trouble fitting the Laplace and gradient images even when directly supervised on them, despite being able to fit images relatively accurately. This may be because the ground truth gradient and Laplace images have many high frequency features which are challenging to represent with any architecture besides SIRENs. In the normalized and colorized images (which PSNR is computed upon), the gradient image fit with ReLU P.E. has “grainy” effects which are more noticeable on gradient and Laplacian images than on natural images.

3.2 Implementation & Reproducibility Details

Data. We use the BSDS500 [33], which we center-crop to 321×321 and resize to 256×256 . The starfish image is the 19th image from this dataset. We will make the bear and pyramid images used in the Poisson image editing experiment publicly available with our code. The ground truth gradient image is computed using the Sobel filter, and is scaled by a constant factor of 10 for training. The ground truth Laplace image is computed using a Laplace filter, and is scaled by a constant factor of 10,000 for training.

Architecture. We use the same 5-layer SIREN MLP for all experiments on fitting images and gradients.

Hyperparameters. We train for 10,000 iterations, and at each iteration fit on every pixel in the gradient or Laplacian image. We use the Adam optimizer with a learning rate of 1×10^{-4} for all experiments, including the Poisson image editing experiments.

Runtime. We train for 10,000 iterations, requiring approximately 90 minutes to fit and evaluate a SIREN.

Hardware. The networks are trained using NVIDIA Quadro RTX 6000 GPUs with 24 GB of memory.

4 Representing Shapes with Signed Distance Functions

We performed an additional baseline using the ReLU positional encoding [35] shown in Figure 4. Similar to the results we obtained using the ReLU positional encoding on images, zero-level set of the SDF, in which the shape is encoded features high-frequencies that are not present while the level of details remains low (despite being much higher than in ReLU, see main paper).

Data. We use the Thai statue from the The Stanford 3D Scanning Repository (<http://graphics.stanford.edu/data/3Dscanrep/>). The room is a Free 3D model from Turbosquid.com. We sample each mesh by subdividing it until we obtain 10 million points and their normals. Those are then converted in .xyz formats we load from our code.

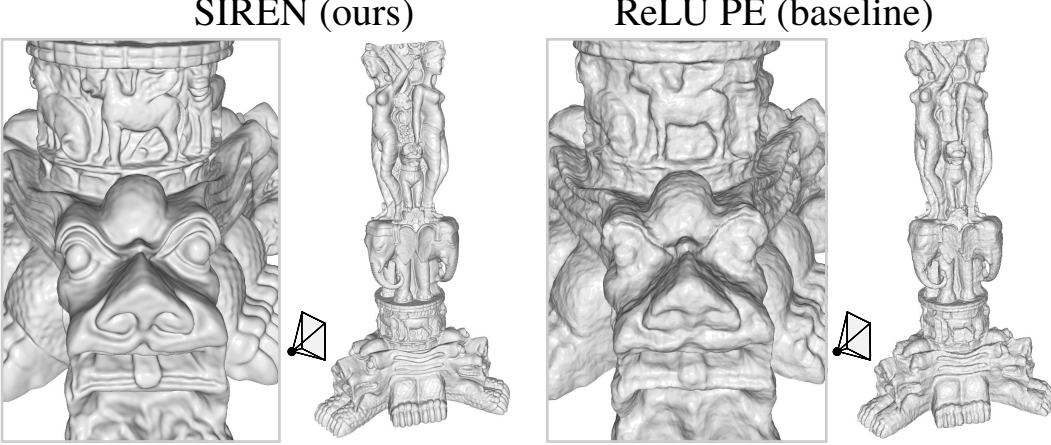


Figure 4: A comparison of SIREN used to fit a SDF from an oriented point cloud against the same fitting performed by an MLP using a ReLU PE (proposed in [35]).

Architecture. We use the same 5-layer SIREN MLP for all experiments on SDF, using 256 units in each layer for the statue and 1024 units in each layer for the room.

Hyperparameters. We train for 50,000 iterations, and at each iteration fit on every voxel of the volume. We use the Adam optimizer with a learning rate of 1×10^{-4} for all experiments. We use the cost described in our paper:

$$\mathcal{L}_{\text{sdf}} = \lambda_1 \int_{\Omega} \| |\nabla_{\mathbf{x}} \Phi(\mathbf{x})| - 1 \| d\mathbf{x} + \int_{\Omega_0} \lambda_2 \|\Phi(\mathbf{x})\| + \lambda_3 (1 - \langle \nabla_{\mathbf{x}} \Phi(\mathbf{x}), \mathbf{n}(\mathbf{x}) \rangle) d\mathbf{x} + \lambda_2 \int_{\Omega \setminus \Omega_0} \psi(\Phi(\mathbf{x})) d\mathbf{x}, \quad (9)$$

with the Eikonal constraint (gradient = 1) multiplied by $\lambda_1 = 5 \cdot 10^1$, the signed distance function constraint as well as the off-surface penalization (the regularizer) multiplied by $\lambda_2 = 3 \cdot 10^3$, and the oriented surface/normal constraint multiplied by $\lambda_3 = 1 \cdot 10^2$.

Runtime. We train for 50,000 iterations, requiring approximately 6h hours to fit and evaluate a SIREN. Though, we remark that SIREN converge already very well after around 5,000-7,000 iterations, much more iterations are needed for the baselines, hence the number of 50,000 iterations.

Hardware. The networks are trained using NVIDIA GTX Titan X GPUs with 12 GB of memory.

5 Solving the Helmholtz and Wave Equations

The Helmholtz and wave equations are second-order partial differential equations related to the physical modeling of diffusion and waves. They are closely related through a Fourier-transform relationship, with the Helmholtz equation given as

$$\underbrace{(\nabla^2 + m(\mathbf{x})w^2)}_{H(m)} \Phi(\mathbf{x}) = -f(\mathbf{x}). \quad (10)$$

Here, $f(\mathbf{x})$ represents a known source function, $\Phi(\mathbf{x})$ is the unknown wavefield, and the squared slowness $m(\mathbf{x}) = 1/c(\mathbf{x})^2$ is a function of the wave velocity $c(\mathbf{x})$. In general, the solutions to the Helmholtz equation are complex-valued and require numerical solvers to compute.

5.1 Helmholtz Perfectly Matched Layer Formulation

To solve the Helmholtz equation uniquely over a finite domain, we use a perfectly matched layer formulation, which attenuates waves on the boundary of the domain. Following Chen et al. [13] we rewrite the Helmholtz equation as

$$\frac{\partial}{\partial x_1} \left(\frac{e_{x_2}}{e_{x_1}} \frac{\partial \Phi(\mathbf{x})}{\partial x_1} \right) + \frac{\partial}{\partial x_2} \left(\frac{e_{x_1}}{e_{x_2}} \frac{\partial \Phi(\mathbf{x})}{\partial x_2} \right) + e_{x_1} e_{x_2} k^2 \Phi(\mathbf{x}) = -f(\mathbf{x}) \quad (11)$$

where $\mathbf{x} = (x_1, x_2) \in \Omega$, $e_{x_i} = 1 - j\frac{\sigma_{x_i}}{\omega}$, $k = \omega/c$, and

$$\sigma_{x_i} = \begin{cases} a_0 \omega \left(\frac{l_{x_i}}{L_{\text{PML}}} \right)^2 & x_i \in \partial\Omega \\ a_0 \omega \left(\frac{l_{x_i}}{L_{\text{PML}}} \right)^2 & \text{else} \end{cases}.$$

Here, a_0 controls the amount of wave attenuation (we use $a_0 = 5$), l_{x_i} is the distance to the PML boundary along the x_i axis, and L_{PML} is the width of the PML. Note that the PML is applied only to the boundary of our domain $\partial\Omega = \{x \mid 0.5 < \|x\|_\infty < 1\}$ and that the equation is identical to the original Helmholtz equation elsewhere. To train SIREN, we optimize Eq. 11 using the loss function described in the main paper with $\lambda(\mathbf{x}) = k = \text{batch size}/5 \times 10^3$.

5.2 Full-Waveform Inversion

For known source positions and sparsely sampled wavefields, full-waveform inversion (FWI) can be used to jointly recover the wavefield and squared slowness over the entire domain. Specifically, FWI involves solving the constrained partial differential equation

$$\arg \min_{m, \Phi} \sum_{1 \leq i \leq N} \int_{\Omega} |\text{III}_r(\Phi_i(\mathbf{x}) - r_i(\mathbf{x}))|^2 d\mathbf{x} \quad \text{s.t.} \quad H(m) \Phi_i(\mathbf{x}) = -f_i(x) \quad 1 \leq i \leq N, \forall \mathbf{x} \in \Omega, \quad (12)$$

where there are N sources, III_r samples the wavefield at the receiver locations, and r_i is the measured receiver data for the i th source.

We solve this equation with a principled method based on the alternating direction method of multipliers [11, 1]. To perform FWI with SIREN, we first pre-train the network to solve for the wavefields given a uniform velocity model. This is consistent with the principled solver, which is initialized with a uniform velocity. This pre-training process updates SIREN to minimize

$$\mathcal{L}_{\text{FWI, pretrain}} = \mathcal{L}_{\text{Helmholtz}} + \lambda_{\text{slowness}} \mathcal{L}_{\text{slowness}} \quad (13)$$

where the first term is as described in the main paper, and the last term is simply $\|m(\mathbf{x}) - m_0\|_1$. $m(\mathbf{x})$ is parameterized using a single output of SIREN and we use an initial squared slowness value of $m_0 = 1$ in our experiments. The loss term $\mathcal{L}_{\text{slowness}}$ is calculated over all sampled locations \mathbf{x} in each minibatch. We also parameterize the multiple wavefields with additional SIREN outputs. This is accommodated in the loss function by sampling all source locations at each optimization iteration and applying the loss function to the corresponding wavefield outputs. Finally, we set $k = \text{batch size}/10^4$ and $\lambda_{\text{slowness}} = \text{batch size}$.

After pre-training, we perform FWI using SIREN with a penalty method variation [43] of Eq. 12 as a loss function. This is formulated as

$$\mathcal{L}_{\text{FWI}} = \mathcal{L}_{\text{Helmholtz}} + \lambda_{\text{data}} \mathcal{L}_{\text{data}} \quad (14)$$

where $\mathcal{L}_{\text{data}} = \sum_i \|\Phi_i(\mathbf{x}) - r_i(\mathbf{x})\|_1 \Big|_{\mathbf{x} \in \Omega_r}$, and Ω_r is the set of receiver coordinates. In other words, we add a weighted loss term using the (PML) Helmholtz formulation on the receiver coordinates. Here we use the same values of k and $\lambda_{\text{slowness}}$ as for pre-training.

5.3 Helmholtz Implementation & Reproducibility Details

Data. The dataset consists of randomly sampled coordinates and a Gaussian source function, as described previously. For neural FWI, the data term of the loss function uses the sampled wavefield values from the output of the principled solver using the same source and receiver locations, but with access to the ground truth velocity.

Architecture. For all Helmholtz experiments, the SIREN architecture (and baselines) use 5 layers with a hidden layer size of 256.

Hyperparameters. We set the loss function hyperparameters to the previously described values in order to make each component of the loss approximately equal during the beginning of training. The Adam optimizer with a learning rate of 2×10^{-5} was used for all experiments.

Runtime. The single-source Helmholtz experiments were trained for 50,000 iterations requiring approximately 3 hours (ReLU), 8 hours (tanh, SIREN), or 24 hours (RBF). For FWI, pretraining required 80,000 (22 hours) iterations in order to suitably fit the 5 wavefields with a single network, and then we performed full-waveform inversion for 10,000 iterations (5 hours) until the loss appeared to converge. We set the batch size to fill the GPU memory; generally, we found that large batch sizes ranging from 3000 to 13000 samples worked well.

Hardware. The experiments are conducted on a NVIDIA Quadro RTX 6000 GPU (24 GB of memory).

5.4 Wave Equation Formulation

The wave equation is given by

$$\frac{\partial \Phi}{\partial t} - c^2 \frac{\partial^2 \Phi}{\partial x^2} = 0. \quad (15)$$

Note that in contrast to the Helmholtz equation, the wave equation is dependent on time. Thus, we parameterize the real-valued wavefield as a function of two spatial dimensions and time: $\Phi(t, \mathbf{x})$. We are interested in solving an initial value problem with the following initial conditions

$$\frac{\partial \Phi(0, \mathbf{x})}{\partial t} = 0 \quad (16)$$

$$\Phi(0, \mathbf{x}) = f(\mathbf{x}). \quad (17)$$

In the case of the acoustic wave equation, the first condition states that the initial particle velocity is zero, and in the second condition, $f(\mathbf{x})$ is an initial pressure distribution.

5.5 Solving the Wave Equation

We solve the wave equation by parameterizing $\Phi(t, \mathbf{x})$ with SIREN. Training is performed on randomly sampled points \mathbf{x} within the domain $\Omega = \{\mathbf{x} \in \mathbb{R}^2 \mid \|\mathbf{x}\|_\infty < 1\}$. The network is supervised using a loss function based on the wave equation:

$$\mathcal{L}_{\text{wave}} = \int_{\Omega} \left\| \frac{\partial \Phi}{\partial t} - c^2 \frac{\partial^2 \Phi}{\partial x^2} \right\|_1 + \lambda_1(\mathbf{x}) \left\| \frac{\partial \Phi}{\partial t} \right\|_1 + \lambda_2(\mathbf{x}) \|\Phi - f(\mathbf{x})\|_1 d\mathbf{x}. \quad (18)$$

Here, λ_1 and λ_2 are hyperparameters, and are non-zero only for $t = 0$. To train the network, we sample values of \mathbf{x} uniformly from Ω and slowly increase the value of t linearly as training progresses, starting from zero. This allows the initial condition to slowly propagate to increasing time values. We set $\lambda_1 = \text{batch size}/100$ and $\lambda_2 = \text{batch size}/10$ and let $c = 1$.

Results are shown in Fig. 5 for solving the wave equation with $f(\mathbf{x})$ equal to a Gaussian centered at the origin with a variance of 5×10^{-4} . We also compare to a baseline network with tanh activations (similar to recent work on neural PDE solvers [37]), and additional visualizations are shown in the video. SIREN achieves a solution that is close to that of a principled solver [40] while the tanh network fails to converge to a meaningful result.

5.6 Wave Equation Implementation & Reproducibility Details

Data. The dataset is composed of randomly sampled coordinates 3D coordinates as described previously. We use a Gaussian source function to approximate a point source, and clip the support to values greater than 1e-5. During training, we scale the maximum value of the Gaussian to 0.02, which we find improves convergence.

Architecture. To fit over the 3 dimensions of the wave equation, we increase the size of the architecture, still using 5 layers, but with a hidden layer size of 512.

Hyperparameters. The loss function hyperparameters are set so that each component of the loss is approximately equal as training progresses. We grow the interval of t from which training coordinates are sampled linearly over 100,000 iterations (roughly 25 hours) from 0.0 to 0.4, which we find allows a sufficient number of iterations for the network to fit the wave function as it expands. For all wave equation experiments, we used the ADAM optimizer and a learning rate of 2×10^{-5} . A batch size of 115,000 is used, which fills the GPU memory.

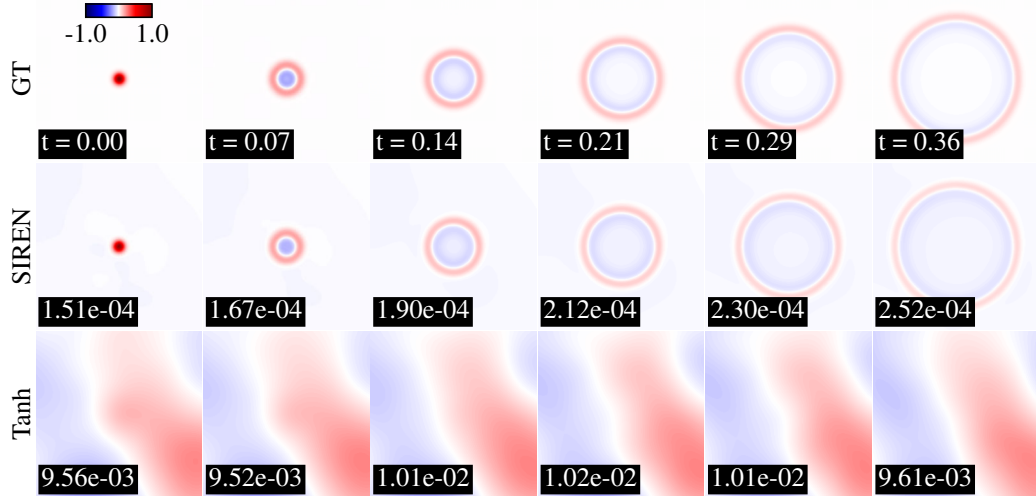


Figure 5: Solving the wave equation initial value problem. For an initial condition corresponding to a Gaussian pulse, SIREN recovers a wavefield that corresponds closely to a ground truth wavefield computed using a principled wave solver [40]. A similar network using tanh activations fails to converge to a good solution. MSE values are shown for each frame, where the time value is indicated in the top row.

Hardware. The experiments are conducted on a NVIDIA Quadro RTX 6000 GPU (24 GB of memory).

6 Application to Image Processing

6.1 Formulation

As shown previously, one example of signal that SIRENs can be used to represent are natural images. A continuous representation of natural images with a SIREN introduces a new way to approach image processing tasks and inverse problems. Consider a mapping from continuous implicit image representation $\Phi(x, y)$ to discrete image b

$$b = \text{III} (h * \Phi_\theta (x, y)), \quad (19)$$

where III is the sampling sampling operator, h is a downsampling filter kernel, and $\Phi(x, y)$ is the continuous implicit image representation defined by its parameters θ . Using this relationship, we can fit a continuous SIREN representation given a discrete natural image b by supervising on the sampled discrete image.

Many image processing problems can be solved by formulating an optimization problem which minimizes data fidelity with partial or noisy measurements of b and some prior over natural images. In our case, our prior is over the space of SIREN representations of natural images. This takes the form:

$$\underset{\{\theta\}}{\text{minimize}} \mathcal{L} (\text{III} (h * \Phi_\theta (x, y)), b) + \lambda \gamma (\Phi_\theta (x, y)), \quad (20)$$

where γ is a regularization function defined on the continuous function, and λ is the weight of the regularizer.

6.2 Image Fitting.

As previously shown, the most simple representation task involves simply fitting an implicit neural representation $\Phi : \mathbb{R}^2 \mapsto \mathbb{R}^3, \mathbf{x} \rightarrow \Phi(\mathbf{x})$ to an image. Simply fitting the image proves to be challenging for many architectures, and fitting higher-order derivatives is only possible using SIRENs. In addition to the comparisons with ReLU, tanh, ReLU P.E., and ReLU with RBF input layer shown in the paper, we show a qualitative comparison with additional neural network architectures in Fig. 6.

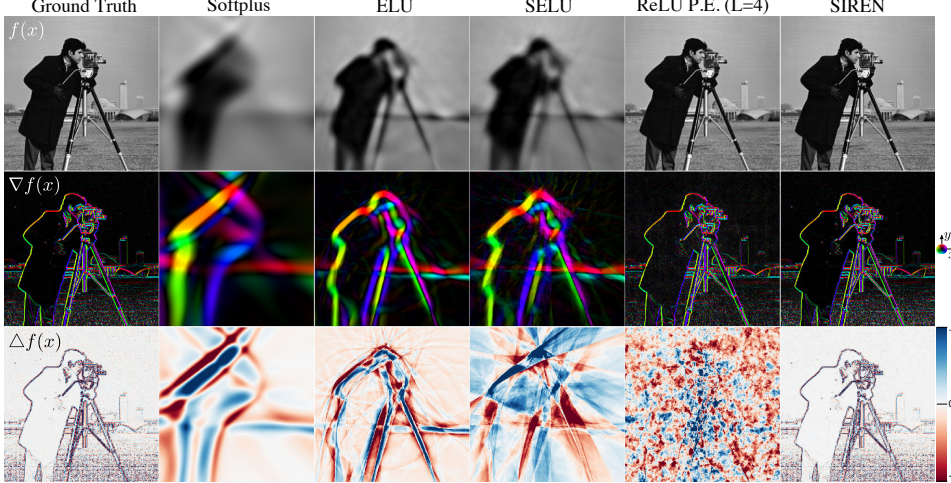


Figure 6: Comparison of different implicit network architectures fitting a ground truth image (top left). The representation is only supervised on the target image but we also show first- and second-order derivatives of the function fit in rows 2 and 3, respectively. We compare with architectures implemented using Softplus, ELU, SELU, and ReLU P.E. ($L=4$) on the cameraman image. The value of L dictates the number of positional encodings concatenated for each input coordinate, and a choice of $L = 4$ was made for images in [35].

6.3 Image Inpainting

Traditional approaches to the single image inpainting task have either focused on diffusion-based [8, 5, 7] or patch based reconstruction [6, 24, 15]. With the advent of deep learning, a slew of new methods have taken advantage of large amounts of data to learn complex statistics of natural images used in reconstruction problems. These inpainting methods are based on convolutional neural networks (CNNs) [27, 38] and generative adversarial networks (GANs) [22, 44, 28, 32]. Additionally, neural network architectures for image recovery like CNNs have been shown to themselves act as a prior [41] for natural images, allowing for solving inverse problems without the use of training data.

We show the capability of SIRENs to solve inverse problems through the example of single image inpainting. By fitting a SIREN to an image and enforcing a prior on the representation, we can solve a single image reconstruction problem. Examples of single image inpainting with and without priors are shown in Fig. 7, where we compare performance on texture images versus Deep Image Prior [41], Navier-Stokes, Fluid Dynamics Image Inpainting [7] (Diffusion), and SIRENs with no prior, total variation prior (TV), and Frobenius norm of Hessian [31, 30] priors (FH) respectively. In Tab. 2, we describe our quantitative results with mean and standard deviation over many independent runs. These results show that SIREN representations can be used to achieve comparable performance to other baseline methods for image inverse problems.

Note that this formulation of loss function can be equivalently formulated in a continuous partial differential equation, and depending on choice of prior, a diffusion based update rule can be derived. For more details on this, see the Rudin–Osher–Fatemi model in image processing [4, 3, 17].

6.4 Implementation & Reproducibility Details

Data. The experiments were run on texture images, including the art image of resolution 513×513 and tiles image of resolution $355 \times 533 \times 3$. These images will be made publicly available with our code. The sampling mask is generated randomly, with an average of 10% of pixels being sampled. We will make the example mask for which these results were generated publicly available with our code. As in all other applications, the image coordinates $\mathbf{x} \in \mathbb{R}^2$ are normalized to be in the range of $[-1, 1]^2$. For evaluation, images are scaled in the range of $[0, 1]$ and larger values are clipped.

Architectures. For the single image inpainting task with SIRENs, we use a 5-layer MLP. For single image fitting on the cameraman image, we use 5-layer MLPs for all activation functions. For the

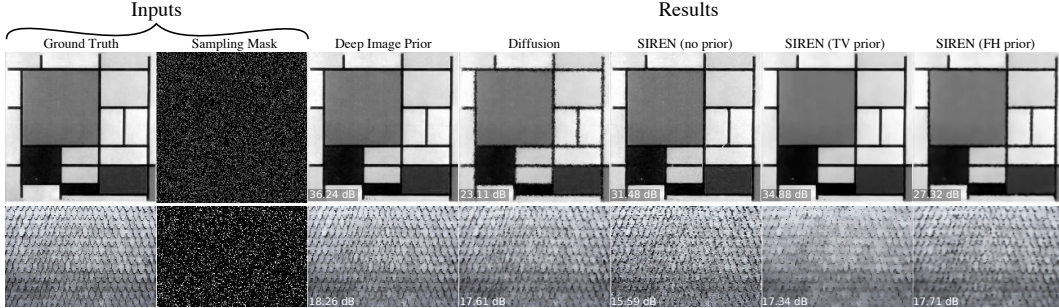


Figure 7: Comparison of various methods and priors on the single image inpainting task. We sample 10% of pixels from the ground truth image for training, learning a representation which can inpaint the missing values. Note that for the image in the first row, where the TV prior is known to be accurate, including the TV prior improves inpainting performance.

RBF-Input and ReLU P.E. models, we add an additional first layer with 256 activations (in the case of RBF-Input) or positional encoding concatenation with positional encoding sinusoid frequencies of $2^i\pi$ for $0 \leq i < L = 7$ (in the case of ReLU P.E.).

Loss Functions. In order to evaluate a prior loss, we must enforce some condition on the higher-order derivatives of the SIREN. This is done by sampling N random points $\mathbf{x}_i \in [-1, 1]^2$, and enforcing the prior on these points. We sample half as many points for the prior as there are pixels in the image. In the case of TV regularization, this consists of a L1 norm on the gradient

$$\gamma_{\text{TV}} = \frac{1}{N} \sum_{i=1}^N |\nabla \Phi_\theta(\mathbf{x}_i)|, \quad (21)$$

while in the case of FH regularization, this consists of L1 norm on all sampled points' Frobenius norm of their Hessian matrix

$$\gamma_{\text{FH}} = \frac{1}{N} \sum_{i=1}^N \|\text{Hess}(\Phi_\theta(\mathbf{x}_i))\|_F. \quad (22)$$

The prior loss is weighted with a regularization weight λ , and combined with the MSE loss on the reconstructed sampled and blurred image points,

$$\mathcal{L}_{\text{img}} = \|\text{III}(h * \Phi_\theta(x, y)) - b\|^2. \quad (23)$$

Downsampling Kernel Implementation. Sampling images from a continuous function requires convolution with a downsampling kernel to blur high frequencies and prevent aliasing. Since we cannot perform a continuous convolution on a SIREN we must instead approximate with Monte Carlo sampling of the SIREN to approximate fitting the blurred function. Consider the 2D image signal where $\mathbf{x} = (x, y)$:

$$(h * \Phi)(x, y) = \int_{x'} \int_{y'} \Phi(x', y') \cdot h(x - x', y - y') dy' dx' \approx \frac{1}{N} \sum_{i=1}^N \Phi(x + x_i, y + y_i) \quad (24)$$

where x_i, y_i are sampled from the kernel h as a normalized probability density function. For example, a bilinear downsampling kernel is given by $h(x, y) = \max(0, 1 - |x|) \max(0, 1 - |y|)$. Thus, we sample x_i, y_i from a probability density function of $p(x_i, y_i) = \frac{1}{2} \max(0, 1 - |x|) \max(0, 1 - |y|)$. In our implementation, we found that not using a downsampling kernel resulted in equivalent performance on the inpainting and image fitting task. However, it may be necessary in cases where we aim to reconstruct our image at multiple resolutions (i.e. superresolution). We only sample one blurred point, i.e. $N = 1$, per iteration and train for many iterations. This is done for computational efficiency, as otherwise it is necessary to backpropagate the loss from all sampled coordinates.

Hyperparameters. For the image fitting experiment, we train all architectures using the Adam optimizer and a learning rate of 1×10^{-4} . Hyperparameters were not rigorously optimized and were

Table 2: Mean and standard deviation of the PSNR of the tiles texture and art texture images for SIRENs with various priors. The statistics are computed over 10 independent runs.

Image	No Prior	No Prior	TV Prior	TV Prior	FH Prior	FH Prior
	Mean PSNR	Std. PSNR	Mean PSNR	Std. PSNR	Mean PSNR	Std. PSNR
Tiles	15.45	0.180	17.40	0.036	17.68	0.051
Art	32.41	0.283	34.44	0.222	27.18	0.116



Figure 8: Example frames from fitting a video with SIREN and ReLU MLPs. SIREN more accurately reconstructs fine details in the video. Mean (and standard deviation) of the PSNR over all frames is reported.

found by random experimentation in the range of $[1 \times 10^{-6}, 1 \times 10^{-4}]$. We train for 15,000 iterations, fitting all pixel values at each iteration.

For the image inpainting experiments, we use the published and OpenCV [12] implementations for the baseline methods, and use an Adam optimizer with a learning rate of 5×10^{-5} for all SIREN methods. We train for 5,000 iterations, fitting all pixel values at each iteration. For the TV prior, we use a regularization weight of $\lambda = 1 \times 10^{-4}$, while for the FH prior, we use a regularization weight of $\lambda = 1 \times 10^{-6}$.

Central Tendencies of Metrics. In Tab. 2, we show the central tendencies (mean and standard deviation) of the quantitative PSNR scores obtained on the image inpainting experiment. Inpainting with SIRENs is highly stable and not sensitive to the specific pixel mask sampled.

Hardware & Runtime. We run all experiments on a NVIDIA Quadro RTX 6000 GPU (24 GB of memory). The single image fitting and regularization experiments require approximately 1 hour to run.

7 Representing Video

We fit videos using SIREN and a baseline ReLU architecture as described in the main paper and video. We also fit a second video, which consists of various vehicles moving in traffic and outdoor scenes, shown in Fig. 8. Again, SIREN shows improved representation of fine details in the scene. In the following we provide additional implementation details.

7.1 Reproducibility & Implementation Details

Data. The first dataset consists of a video of a cat, which is permissively licensed and available at the time of this writing from <https://www.pexels.com/video/the-full-facial-features-of-a-pet-cat-3040808/>. The second dataset is the “bikes sequence” available from the scikit-video Python package described here <http://www.scikit-video.org/stable/datasets.html>. We crop and downsample the cat video to 300 frames of 512×512 resolution. The second dataset consists of 250 frames fit at the original resolution of 272×640 pixels.

Architecture. The SIREN and ReLU architectures use 5 layers with a hidden layer size of 1024.

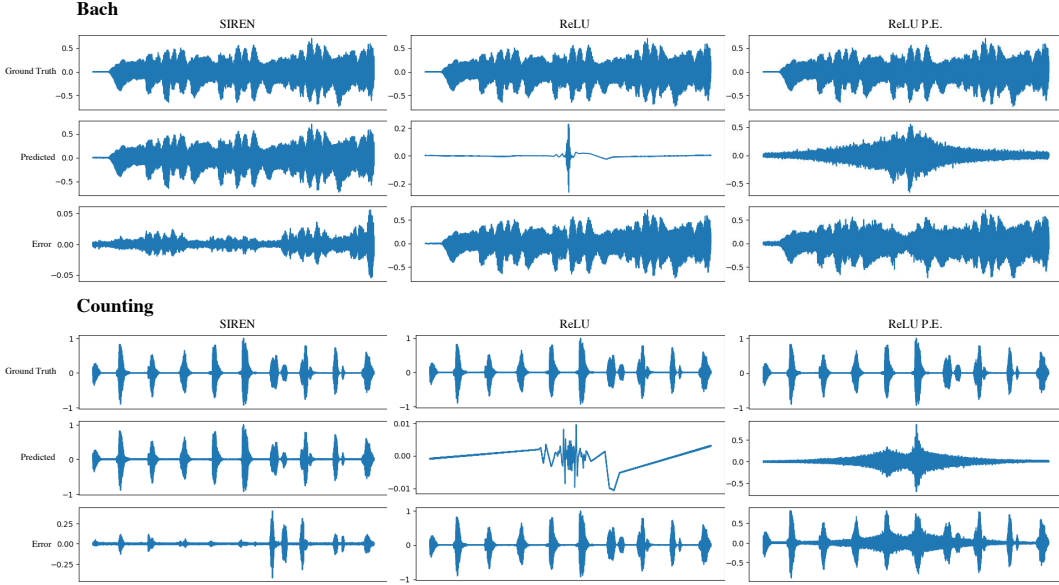


Figure 9: Fitted waveforms and error for various implicit neural representation architectures. We fit the network to the first 7 seconds of Bach’s Cello Suite No. 1: Prelude (Bach) and to a 12 second clip of a male actor counting 0-9 (Counting). Only SIREN representations capture the waveform structure.

Hyperparameters. The Adam optimizer with a learning rate of 1×10^{-4} was used for all experiments. We set the batch size to fill the memory of the GPUs (roughly 160,000).

Runtime. We train the videos for 100,000 iterations, requiring approximately 15 hours.

Hardware. The networks are trained using NVIDIA Titan X (Pascal) GPUs with 12 GB of memory.

8 Representing Audio Signals

Various methods exist for audio signal representation. Early work consists of representing audio signals using various spectral features [25, 9, 23]. Spectrograms, representations of the spectrum of frequencies of a signal as it varies with time, have been used in machine learning applications due to the ease of applying widely successful image processing CNN architectures to them [21, 14, 39]. More recently, neural network architectures have been developed which can operate on raw audio waveforms [42, 14, 34].

To demonstrate the versatility of SIRENs as implicit neural representations, we show that they can efficiently model audio signals. Due to the highly periodic nature of audio signals with structure at various time scales, we expect that SIRENs could accurately represent such signals efficiently and provide an alternative representation for audio signals. We evaluate SIREN performance on raw audio waveforms of varying length clips of music and speech. While other neural network architectures fail to accurately model waveforms, SIRENs are able to quickly converge to a representation which can be replayed with minimal distortion. We fit a SIREN to a sampled waveform a using a loss of the form:

$$\mathcal{L} = \int_{\Omega} \| \text{III}_a(\Phi(\mathbf{x})) - a(\mathbf{x}) \|^2 d\mathbf{x}. \quad (25)$$

where III_a samples the SIREN at the waveform measurement locations.

Fig. 9 displays the fit waveform to music and speech data respectively. We see that other neural network architectures are not able to represent raw audio waveforms at all, while SIRENs produce an accurate waveform. Additionally, we note that the number of parameters in our SIREN is far less than the number of samples in the ground truth waveform. This ability to compress signals supports our claim that periodic SIREN representations are well suited to representing audio signals, and perhaps

Table 3: Mean squared error of representing the raw audio waveform scaled in the range $[-1, 1]$ with a SIREN. The mean and variance of the reconstruction MSE are evaluated over 10 independent runs of fitting. Each architecture is fitted for 5000 iterations.

Architecture	Bach		Counting	
	MSE Mean	MSE Standard Dev.	MSE Mean	MSE Standard Dev.
ReLU	2.504×10^{-2}	1.706×10^{-3}	7.466×10^{-3}	8.217×10^{-5}
ReLU P.E.	2.380×10^{-2}	3.946×10^{-4}	9.078×10^{-3}	9.627×10^{-4}
SIREN	1.101×10^{-5}	2.539×10^{-6}	3.816×10^{-4}	1.632×10^{-5}

lossy compression algorithms for audio could be designed using SIRENs. Our supplemental video contains audio from the SIREN, which is accurate and recognizable. Tab. 3 shows the converged SIREN mean-squared error on the original audio signal and statistics on these metrics (these were feasible to evaluate due to the relatively short training time of SIRENs on audio signals). This shows SIRENs are highly stable in convergence.

8.1 Reproducibility & Implementation Details

Data. For music data, we use the first 7 seconds from Bach’s Cello Suite No. 1: Prelude available at <https://www.yourclassical.org/story/2017/04/04/daily-download-js-bach--cello-suite-no-1-prelude> and for the speech we use stock audio of a male actor counting from 0 to 9 available at <http://soundbible.com/2008-0-9-Male-Vocalized.html>. These waveforms have a sampling rate of 44100 samples per second. As pre-processing, they are normalized to be in the range of $[-1, 1]$. We use the entire set of samples to fit our SIREN in each batch.

Architecture. We use the same 5-layer MLP with sine nonlinearities as for all other SIREN applications.

Frequency Scaling. To account for the high sampling rate of audio signals, we scale the domain $\mathbf{x} \in [-100, 100]$ instead of $[-1, 1]$. This is equivalent to adding a constant multiplication term to the weights of the input layer of the SIREN.

Hyperparameters. We use the Adam optimizer with a learning rate of 5×10^{-5} to generate the results. We evaluated both learning rates of 5×10^{-5} and 1×10^{-4} , finding that 5×10^{-5} worked slightly better. We train for 9,000 iterations for the figures generated, and 5,000 iterations for the quantitative results listed in the table (the model is largely converged after only 2,000 iterations).

Hardware & Runtime. The experiments are conducted on a NVIDIA Quadro RTX 6000 GPU (24 GB of memory), where training for 9000 iterations takes roughly 20 minutes for the Bach signal and 30 minutes for the counting signal.

9 Learning a Space of Implicit Functions

A strong prior over the space of SIREN functions enables applications such as reconstruction from noisy or few observations. We demonstrate that this can be done over the function space of SIRENs representing faces in the CelebA dataset [29]. We use the learned prior to perform image inpainting of missing pixels.

9.1 Reproducibility & Implementation Details

Data. Partial observations (referred to as context) of the input image consist of coordinates and pixel values $O = \{(x_i, c_i)\}_{i=0}^N$ sampled from an image $b \in \mathbb{R}^{H \times W \times 3}$. Like in [16], $b \in \mathbb{R}^{32 \times 32 \times 3}$ is center-cropped and downsampled from the images in the CelebA training dataset, containing 162,770 images. We evaluate our test performance on a similarly center-cropped and downsampled version of the CelebA test dataset, containing 19,962 images.

Context Encoder. The results presented in the main paper use a convolutional neural network encoder which operates on sparse images. More specifically, the partial observations are combined into sparse images $O \in \mathbb{R}^{32 \times 32 \times 3}$, where observed pixel locations are either their value c_i and masked pixel locations are given a value of 0. The encoder C operates on these sparse images, and is parameterized as a standard convolutional neural network (CNN) with an input convolutional layer followed by four residual blocks with ReLU nonlinearities. Each intermediate feature map has 256 channels. This outputs per-pixel embeddings in \mathbb{R}^{256} , which are aggregated together into a single context embedding using a fully connected layer.

We also describe the use of a set encoder as in [16] for encoding the partial observations. In this case, partial observations consist of a list of coordinates and pixel values $O = \{(x_i, c_i)\}_{i=0}^N, (x_i, c_i) \in \mathbb{R}^5$. The encoder C is an MLP which operates on each of these observations independently. The MLP consists of two hidden layers with sine nonlinearities, and outputs an embedding per pixel in \mathbb{R}^{256} . The embeddings are aggregated together using a mean operation. Since each embedding depends only on the context pixel, and the mean operation is symmetric, this set encoder is permutation invariant.

We consider one final encoder C based on partial convolutions [27]. Partial convolutions are designed to operate on sparse images, conditioning outputs of each layer only on valid input pixels. In this case, the partial observations are combined into a sparse image and mask, much like in the CNN encoder case. However, the encoder is implemented using an input partial convolution followed by four partial convolution residual layers with ReLU nonlinearities. Each intermediate map also has 256 channels. The output per-pixel embeddings are similarly aggregated together into a single context embedding using a fully connected layer.

Hypernet. We use a hypernet as our decoder, which maps the latent code to the weights of a 5-layer SIREN with hidden features of size 256 (as in all other experiments). This hypernet is a ReLU MLP with one hidden layer with 256 hidden features.

Loss Function. We train the encoder C and hypernet Ψ operating on context O by minimizing the loss function:

$$\mathcal{L} = \underbrace{\frac{1}{HW} \|\Phi(\mathbf{x}) - b\|_2^2}_{\mathcal{L}_{\text{img}}} + \lambda_1 \underbrace{\frac{1}{k} \|z\|_2^2}_{\mathcal{L}_{\text{latent}}} + \lambda_2 \underbrace{\frac{1}{l} \|\theta\|_2^2}_{\mathcal{L}_{\text{weights}}} \quad (26)$$

where (H, W) are the spatial dimensions of the images in the dataset, $\Phi = (\Psi \circ C)(O)$ is the predicted SIREN representation from the hypernet, b is the ground truth image, k is the dimensionality of the embedding z , and l is the amount of weights Φ in the SIREN Φ .

\mathcal{L}_{img} enforces the closeness of image represented by the SIREN to ground-truth, $\mathcal{L}_{\text{latent}}$ enforces a Gaussian prior on latent code z , and $\mathcal{L}_{\text{weights}}$ is a regularization term on the weights of Φ which can be interpreted as encouraging a lower frequency representation of the image. The regularization terms are necessary since there are many possible SIREN representations for an image, so we need to encourage unique solutions (lowest possible frequency) which lie in a more compact latent space (Gaussian). For all of our results, we use regularization weighting parameters of $\lambda_1 = 1 \times 10^{-1}$ and $\lambda_2 = 1 \times 10^2$.

Hypernet Initialization. In order to improve performance, we devise a heuristic initialization scheme for the hypernet which deviates from the default Kaiming initialization for ReLU MLP networks [20]. Although a formal theoretical analysis of this initialization has not been well studied, we found that the initialization led to convergence of our encoder and hypernet models. We only modify the default ReLU MLP initialization in the final layer of the hypernet by scaling the Kaiming initialized weights by 1×10^{-2} , and initializing the biases uniformly in the range of $[-1/n, 1/n]$ where n is the number of inputs to the layer of the SIREN being predicted.

The motivation for this scheme is that the initialization of the biases of the hypernet is a heuristic initialization of SIRENs which leads to high quality convergence results. Thus, initializing the weights of the hypernet with a small magnitude ensures that the SIREN weights outputted at initialization of the hypernet are close to a initialization of a single SIREN, regardless of input to the hypernet.



Figure 10: Additional results using the CNN encoder with hypernetwork decoder.

Training Procedure. In order to encourage invariance to the number of partial observations, we randomly sample from 10 to 1000 context pixels to input into the convolutional or partial convolutional encoder. In the case of the set encoder which is permutation invariant, we mimic the training procedure of [16] by varying from 10 to 200 sampled context pixels.

Hyperparameters. As mentioned, we use loss parameters $\lambda_1 = 1 \times 10^{-1}$ and $\lambda_2 = 1 \times 10^2$. For all experiments, we use the Adam optimizer with a learning rate of 5×10^{-5} , a batch size of 200 images, and train for 175 epochs on the training dataset. We found these hyperparameters by trial and error, having tested values of $\lambda_1 \in [10^{-3}, 10^{-1}]$, $\lambda_2 \in [10^1, 10^4]$, learning rates of $5 \times 10^{-5}, 1 \times 10^{-4}$, and a batch size of 200 and 1000.

Runtime. We train the videos for 175 epochs on the downsampled CelebA training set, requiring approximately 24 hours.

Hardware. The networks are trained using NVIDIA Quadro RTX 6000 GPUs with 24 GB of memory.

9.2 Additional Results

We show additional results from the convolutional encoder in Fig. 10

We also show results from the set encoder with sine nonlinearities in Fig. 11, set encoder with ReLU nonlinearities (as in the original CNP architecture) in Fig. 12, and convolutional encoder based on partial convolutions in Fig. 13. All of these implementations use the same hypernetwork architecture as a decoder from latent codes to SIREN weights. Tab. 4 shows comparisons between architectures for the encoder.

Interestingly, the partial convolutional encoder performs worse than both the set encoders and convolutional encoder. We suspect that the convolutional encoder has an easier time capturing complex spatial relationships between the context pixels and using information from the masked pixels instead of only conditioning on valid pixels. Regardless of encoder architecture, some prior



Figure 11: Additional results using the set encoder with sine nonlinearities with a hypernetwork decoder.

Table 4: Quantitative comparison of inpainting on the CelebA test dataset. Metrics are reported in pixel-wise mean squared error for varying numbers of context pixels. All of the methods for generalizing over SIRENs use a hypernetwork as a decoder from latent code to SIREN weights. CNP does not report quantitative metrics on half or full images given as context.

Number of Context Pixels	10	100	1000	512 (Half)	1024
CNP [16]	0.039	0.016	0.009	-	-
Sine Set Encoder + Hypernet.	0.035	0.013	0.009	0.022	0.009
ReLU Set Encoder + Hypernet.	0.040	0.018	0.012	0.026	0.012
PConv CNN Encoder + Hypernet.	0.046	0.020	0.018	0.060	0.019
CNN Encoder + Hypernet.	0.033	0.009	0.008	0.020	0.008

over the space of SIRENs has been learned which can be used to perform inpainting comparably to methods such as CNP [16] operating on images directly.

10 References

- [1] H. S. Aghamiry, A. Gholami, and S. Operto. Improving full-waveform inversion by wavefield reconstruction with the alternating direction method of multipliers. *Geophysics*, 84(1):R139–R162, 2019.
- [2] R. B. Ash, B. Robert, C. A. Doleans-Dade, and A. Catherine. *Probability and measure theory*. Academic Press, 2000.
- [3] G. Aubert and J.-F. Aujol. Modeling Very Oscillating Signals. Application to Image Processing. *Applied Mathematics and Optimization*, 51:163—182, 2005.
- [4] G. Aubert and P. Kornprobst. *Mathematical Problems in Image Processing: Partial Differential Equations and the Calculus of Variations*. Springer Publishing Company, Incorporated, 2nd edition, 2010.
- [5] C. Ballester, M. Bertalmio, V. Caselles, G. Sapiro, and J. Verdera. Filling-in by joint interpolation of vector fields and gray levels. *IEEE Trans. on Image Processing*, 10(8):1200–1211, 2001.
- [6] C. Barnes, E. Shechtman, A. Finkelstein, and D. B. Goldman. Patchmatch: A randomized correspondence algorithm for structural image editing. *ACM Trans. on Graphics*, 28(3), 2009.



Figure 12: Additional results using the set encoder with ReLU nonlinearities with a hypernetwork decoder.

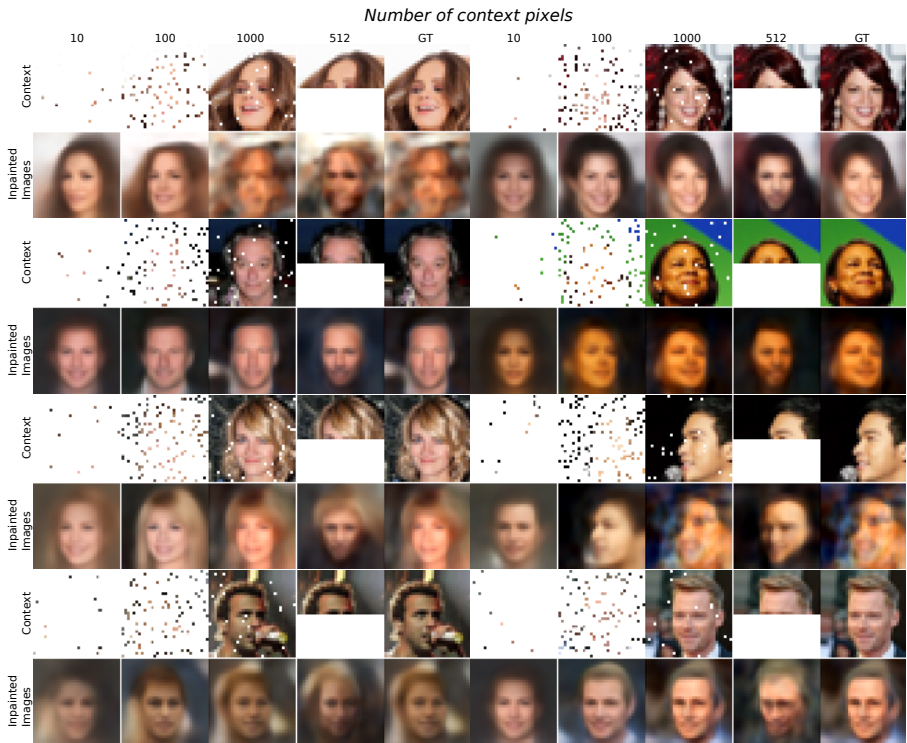


Figure 13: Additional results using a CNN with partial convolution encoder with a hypernetwork decoder.

- [7] M. Bertalmio, A. L. Bertozzi, and G. Sapiro. Navier-stokes, fluid dynamics, and image and video inpainting. In *Proc. CVPR*, volume 1, 2001.
- [8] M. Bertalmio, G. Sapiro, V. Caselles, and C. Ballester. Image inpainting. In *Proc. Annual Conference on Computer Graphics and Interactive Techniques*, page 417–424, 2000.
- [9] A. Bertrand, K. Demuynck, V. Stouten, and H. Van hamme. Unsupervised learning of auditory filter banks using non-negative matrix factorisation. In *Proc. ICASSP*, pages 4713–4716, 2008.
- [10] S. R. Bowling, M. T. Khasawneh, S. Kaewkuekool, and B. R. Cho. A logistic approximation to the cumulative normal distribution. *Journal of Industrial Engineering and Management*, 2(1), 2009.
- [11] S. Boyd, N. Parikh, E. Chu, B. Peleato, J. Eckstein, et al. Distributed optimization and statistical learning via the alternating direction method of multipliers. *Foundations and Trends® in Machine learning*, 3(1):1–122, 2011.
- [12] G. Bradski. The OpenCV Library. *Dr. Dobb's Journal of Software Tools*, 2000.
- [13] Z. Chen, D. Cheng, W. Feng, and T. Wu. An optimal 9-point finite difference scheme for the helmholtz equation with pml. *International Journal of Numerical Analysis & Modeling.*, 10(2), 2013.
- [14] C. Donahue, J. McAuley, and M. Puckette. Adversarial audio synthesis. In *Proc. ICLR*, 2019.
- [15] A. A. Efros and W. T. Freeman. Image quilting for texture synthesis and transfer. In *Proc. Conference on Computer Graphics and Interactive Techniques*, SIGGRAPH '01, page 341–346, 2001.
- [16] M. Garnelo, D. Rosenbaum, C. J. Maddison, T. Ramalho, D. Saxton, M. Shanahan, Y. W. Teh, D. J. Rezende, and S. Eslami. Conditional neural processes. *arXiv preprint arXiv:1807.01613*, 2018.
- [17] P. Getreuer. Rudin-Osher-Fatemi Total Variation Denoising using Split Bregman. *Image Processing On Line*, 2:74–95, 2012.
- [18] X. Glorot and Y. Bengio. Understanding the difficulty of training deep feedforward neural networks. In *Proceedings of the thirteenth international conference on artificial intelligence and statistics*, pages 249–256, 2010.
- [19] L. A. Goodman. On the exact variance of products. *Journal of the American statistical association*, 55(292):708–713, 1960.
- [20] K. He, X. Zhang, S. Ren, and J. Sun. Delving deep into rectifiers: Surpassing human-level performance on imagenet classification. In *Proc. ICCV*, pages 1026–1034, 2015.
- [21] S. Hershey, S. Chaudhuri, D. P. W. Ellis, J. F. Gemmeke, A. Jansen, R. C. Moore, M. Plakal, D. Platt, R. A. Saurous, B. Seybold, M. Slaney, R. J. Weiss, and K. Wilson. Cnn architectures for large-scale audio classification. In *Proc. ICASSP*, pages 131–135, 2017.
- [22] S. Iizuka, E. Simo-Serra, and H. Ishikawa. Globally and Locally Consistent Image Completion. *ACM Trans. on Graphics*, 36(4):107:1–107:14, 2017.
- [23] Q. Kong, Y. Xu, W. Wang, and M. D. Plumbley. Audio set classification with attention model: A probabilistic perspective. In *Proc. ICASSP*, pages 316–320, 2018.
- [24] V. Kwatra, I. Essa, A. Bobick, and N. Kwatra. Texture optimization for example-based synthesis. *ACM Trans. on Graphics*, 24(3):795–802, 2005.
- [25] H. Lee, P. Pham, Y. Largman, and A. Y. Ng. Unsupervised feature learning for audio classification using convolutional deep belief networks. In Y. Bengio, D. Schuurmans, J. D. Lafferty, C. K. I. Williams, and A. Culotta, editors, *Proc. NIPS*, pages 1096–1104. 2009.
- [26] J. W. Lindeberg. Eine neue herleitung des exponentialgesetzes in der wahrscheinlichkeitsrechnung. *Mathematische Zeitschrift*, 15(1):211–225, 1922.
- [27] G. Liu, F. A. Reda, K. J. Shih, T.-C. Wang, A. Tao, and B. Catanzaro. Image inpainting for irregular holes using partial convolutions. In *Proc. ECCV*, September 2018.
- [28] H. Liu, B. Jiang, Y. Xiao, and C. Yang. Coherent semantic attention for image inpainting. In *Proc. ICCV*, July 2019.
- [29] Z. Liu, P. Luo, X. Wang, and X. Tang. Deep learning face attributes in the wild. In *Proc. ICCV*, December 2015.
- [30] M. Lysaker. Iterative image restoration combining total variation minimization and a second-order functional. *International Journal of Computer Vision*, 66:5–18, 2006.
- [31] M. Lysaker, A. Lundervold, and Xue-Cheng Tai. Noise removal using fourth-order partial differential equation with applications to medical magnetic resonance images in space and time. *IEEE Trans. on Image Processing*, 12(12):1579–1590, 2003.
- [32] Y. Ma, X. Liu, S. Bai, L. Wang, A. Liu, D. Tao, and E. Hancock. Region-wise generative adversarial image inpainting for large missing areas, 2019.

- [33] D. Martin, C. Fowlkes, D. Tal, and J. Malik. A database of human segmented natural images and its application to evaluating segmentation algorithms and measuring ecological statistics. In *Proc. ICCV*, July 2001.
- [34] S. Mehri, K. Kumar, I. Gulrajani, R. Kumar, S. Jain, J. Sotelo, A. C. Courville, and Y. Bengio. Samplernn: An unconditional end-to-end neural audio generation model. In *Proc. ICLR*, 2017.
- [35] B. Mildenhall, P. P. Srinivasan, M. Tancik, J. T. Barron, R. Ramamoorthi, and R. Ng. Nerf: Representing scenes as neural radiance fields for view synthesis. *arXiv preprint arXiv:2003.08934*, 2020.
- [36] J. M. H. Olmsted. *Real variables: An introduction to the theory of functions*. Appleton-Century-Crofts, 1959.
- [37] M. Raissi, P. Perdikaris, and G. E. Karniadakis. Physics-informed neural networks: A deep learning framework for solving forward and inverse problems involving nonlinear partial differential equations. *Journal of Computational Physics*, 378:686–707, 2019.
- [38] Y. Ren, X. Yu, R. Zhang, T. H. Li, S. Liu, and G. Li. Structureflow: Image inpainting via structure-aware appearance flow. In *Proc. ICCV*, 2019.
- [39] J. Shen, R. Pang, R. J. Weiss, M. Schuster, N. Jaitly, Z. Yang, Z. Chen, Y. Zhang, Y. Wang, R. Skerrv-Ryan, R. A. Saurous, Y. Agiomvrgiannakis, and Y. Wu. Natural tts synthesis by conditioning wavenet on mel spectrogram predictions. In *Proc. ICASSP*, pages 4779–4783, 2018.
- [40] B. E. Treeby and B. T. Cox. k-wave: Matlab toolbox for the simulation and reconstruction of photoacoustic wave fields. *Journal of biomedical optics*, 15(2):021314, 2010.
- [41] D. Ulyanov, A. Vedaldi, and V. Lempitsky. Deep image prior, 2018.
- [42] A. van den Oord, S. Dieleman, H. Zen, K. Simonyan, O. Vinyals, A. Graves, N. Kalchbrenner, A. Senior, and K. Kavukcuoglu. WaveNet: A Generative Model for Raw Audio. In *Arxiv*, 2016.
- [43] T. Van Leeuwen and F. J. Herrmann. Mitigating local minima in full-waveform inversion by expanding the search space. *Geophysical Journal International*, 195(1):661–667, 2013.
- [44] J. Yu, Z. Lin, J. Yang, X. Shen, X. Lu, and T. S. Huang. Free-form image inpainting with gated convolution. In *Proc. ICCV*, October 2019.